Mapping technique for stellarators

S. V. Kasilov
Institute of Plasma Physics, National Science Center "Kharkov Institute of Physics and Technology," Akademicheskaya Str. 1, 61108 Kharkov, Ukraine

W. Kernbichler[a]
Institut für Theoretische Physik, Technische Universität Graz, Petersgasse 16, A-8010 Graz, Austria

V. V. Nemov
Institute of Plasma Physics, National Science Center "Kharkov Institute of Physics and Technology," Akademicheskaya Str. 1, 61108 Kharkov, Ukraine

M. F. Heyn
Institut für Theoretische Physik, Technische Universität Graz, Petersgasse 16, A-8010 Graz, Austria

The Stochastic Mapping Technique (SMT), a highly efficient method to solve the five-dimensional drift kinetic equation in the long-mean-free-path regime, is presented in an application to stellarators. Within this method, the dimensionality of the problem is reduced to four dimensions through a discretization in one dimension. Instead of tracing test particles in the whole phase space, test particles are followed on particular Poincaré cuts. With this approach, the computation time is reduced by a large factor compared to direct Monte Carlo methods. The SMT is applicable to stellarators with arbitrary magnetic field geometries and topologies. It can be used for any problem where currently conventional Monte Carlo methods are applied. In particular, it is well suited for modeling the distribution function of supra-thermal particles generated by auxiliary heating methods, for studies of stellarator transport properties and for a fast survey of a specific configuration in the whole phase space necessary for an estimation of α-particle confinement. © *2002 American Institute of Physics.* [DOI: 10.1063/1.1493793]

I. INTRODUCTION

Particle methods are powerful modern tools for computer modeling of various kinetic phenomena in plasmas. They can be used to compute the distribution function itself as well as different macroscopic parameters of the plasma. The essence of these methods is based on the definition of the distribution function as the particle density in phase space. Thus, following the orbits of "all" plasma particles is the same as modeling the distribution function. Naturally, it is impossible and also not necessary at all to follow literally all possible orbits of the real particles. Instead, a relatively small number of "test" particles is sufficient for that purpose. The main requirement is that this number is large enough to ensure the presence of a sufficient number of test particles in each "elementary" volume of phase space. Such an elementary volume should on one hand be small enough compared to the scale of the distribution function and on the other hand it should be not too small in order to keep the overall number of test particles below a reasonable limit.

In nonaxisymmetric systems, the drift kinetic equation (DKE) governing the particle evolution is five-dimensional. To meet the first requirement in such a high dimensional phase space, the amount of test particles has to be big. In addition, the time to follow test particles is of the order of the relaxation times of macroscopic parameters. Typically, this is much longer than the characteristic time scale of the individual particle motion. In the case of the DKE, the time scale of particle motion is in the range of either the bounce time or the collision time which are certainly much smaller than a typical relaxation time.

In addition to this, modern stellarators have a quite complex magnetic field geometry where numerous toroidal and poloidal modes contribute to the magnetic field spectrum. This makes a direct computation of the field and of the drift orbits "expensive" in terms of computing time. In addition, the restriction to a Fourier representation in flux coordinates does not allow for a proper treatment of such real space configurations which besides embedded surfaces also include island structures or ergodic zones.

Therefore, it is of high interest to develop a method which allows for a proper treatment of general magnetic configurations. The Stochastic Mapping Technique (SMT) is such a method to solve the DKE in the long mean free path regime. The method is capable of dealing with a general magnetic-field geometry in real space coordinates and shows a strong gain in computational speed making use of a discretization in one dimension, of local magnetic coordinate systems, of precomputed maps for the magnetic field and for drift orbits, and of a proper stochastic treatment of Coulomb collisions.

In the present paper, the SMT for stellarators is described in detail, various applications of this technique are discussed and the results of benchmarking with other meth-

---

[a]Electronic mail: kernbichler@itp.tu-graz.ac.at

ods are presented. Basically, the applications of SMT are the same as of conventional Monte Carlo (MC) methods.[1] In addition, various weighting schemes developed for conventional Monte Carlo methods are fully applicable to SMT. On the other hand, the high computational speed gained with SMT (2 orders of magnitude or more) allows for the solution of problems where the usage of conventional MC methods is not reasonable because of large computation times.

The main idea behind SMT to replace the continuous particle motion with a sequence of mappings of particle footprints is definitely not new. For example, the motion of passing particles in the ergodic field of a stellarator has been modeled in this way in Ref. 2. In this reference, the Coulomb collisions have been modeled with random changes of velocity space variables correctly in a qualitative way. The idea to use numerically computed orbits for the construction of Poincaré maps has been applied to model the regular motion of run-away electrons in Refs. 3 and 4. However, in the present approach, for the first time, the treatment of collision processes and the usage of real drift orbits for the construction of Poincaré maps are performed consistently for the DKE. The formalism allowing for such a consistent treatment has been developed in Ref. 5.

In Sec. II A, a convenient formulation of the DKE in tensor notation and of the set of equations governing the dynamics of drift particle motion is given. In Sec. II B, the concept of the SMT is discussed. In the long-mean-free-path regime, velocity space diffusion and inelastic processes (right-hand side of the DKE) produce only small changes of the distribution function within one ''bounce'' time and, therefore, stochastic orbits can be discretized with respect to one of the phase space variables. For this purpose, Poincaré cuts are introduced and the concept of a regular map for drift orbits and of a stochastic map including all random perturbations is discussed. In Appendix A, it is briefly outlined how to transform the DKE to an integral equation describing the conservation of a pseudo-scalar particle flux density. In Sec. II C, an appropriate Monte Carlo method to solve this second kind Fredholm integral equation by averaging over Markov chains is described.

In Sec. III A and Appendix B, the concept of local magnetic coordinate systems[6] is introduced. This concept allows for a clear separation of slow cross-field transport from the fast parallel motion, and thus strongly reduces the problem of numerical diffusion and pertinent memory requirements. In Sec. III B, a small Larmor radius approximation for displacements of the footprints on the Poincaré cuts due to magnetic and electric drifts is introduced. These displacements can be presented in the form of a Taylor series up to second order in the Larmor radius expansion. The expansion coefficients are three-dimensinal functions of the position on the cut and of the particle pitch. This keeps the memory requirement in a reasonable range. Moreover, the dependence on the radial electric field is of parametric type only. Therefore, iterations with varying electrostatic potential can be done without recomputing the maps.

In Sec. III C, a simplified Coulomb collision operator taking into account velocity space effects only is introduced. Again, the orbit integrated components of the diffusion ten-

sor and of the drag force have to be stored in three dimensions where the main effort is to reconstruct the dependence on the particle pitch. The dependence on the momentum modulus can be easily factorized.

In Appendix C, it is shown how the distribution function can be reconstructed in every spatial point of the configuration. In addition, formulas for various moments of the distribution function are presented.

In Sec. IV, the SMT is applied to the problem of computing neoclassical transport coefficients and to the ''global'' problem of computing convective fluxes generated by suprathermal particles in a stellarator.[7–9] Two magnetic configurations have been considered, the Wendelstein 7-AS (W7-AS) stellarator[10] and the quasi-helically symmetric stellarator (QHS).[11] The first configuration has a rather complicated topology of the minimum-B surfaces, whereas the second one is very sensitive to the accuracy of particle drift modeling. For both configurations, a real space representation of the magnetic field has been used. For QHS, the expansion over the associated Legendre functions[12] has been applied.

II. GENERAL FORMALISM

A. Drift kinetic equation

The drift-kinetic equation for the particle distribution function $f(\mathbf{z})$ in tensor notation has the form

$$V^i \frac{\partial f}{\partial z^i} = \frac{1}{J} \frac{\partial}{\partial z^i} J \left(D^{ij} \frac{\partial f}{\partial z^j} - F^i f \right) - \nu f + Q. \tag{1}$$

The set of variables $\mathbf{z}$ includes the guiding center coordinates in some general curvilinear coordinate system, $z^i = x^i$ with $i = 1 \ldots 3$, the momentum space variables, $z^4 = |\mathbf{p}|$, and, $z^5 = \lambda = p_\| / |\mathbf{p}|$, being the momentum modulus and pitch, respectively, and the time, $z^6 = t$. Also, V^i is the velocity of the guiding center motion in coordinate-momentum-time space (phase-time space)

$$D^{ij} = D^{ij}(\mathbf{z}) = D^{ij}_C + D^{ij}_{QL},$$

$$F^i = F^i(\mathbf{z}) = F^i_C + F^i_{QL}, \tag{2}$$

are the components of the diffusion tensor and of the friction force, respectively, describing both the effects of Coulomb collisions and of quasi-linear diffusion due to rf-heating, $\nu = \nu(\mathbf{z})$ is the particle sink rate due to inelastic processes, $Q = Q(\mathbf{z})$ is a particle source, and J is the Jacobian of the coordinates $(\mathbf{z}, \phi)$ with ϕ being the gyro-phase

$$J = \left| \frac{\partial(\mathbf{r}, \mathbf{p}, t)}{\partial(\mathbf{z}, \phi)} \right| = \sqrt{g} \frac{B^*_\|(\mathbf{z})}{B(\mathbf{x})} p^2, \tag{3}$$

where[13,14]

$$B^*_\|(\mathbf{z}) = h_i B^{*i}, \quad B^{*i} = B^i + \frac{c}{e} \frac{p\lambda}{\sqrt{g}} \varepsilon^{ijk} \frac{\partial h_k}{\partial x^j}. \tag{4}$$

Here, e, c, $\sqrt{g}$, B^i, and h_i, are particle charge, speed of light, metric determinant of spatial coordinate system $\mathbf{x}$, contravariant components of the magnetic field and covariant

components of the unit vector along the magnetic field $\mathbf{h}$ $=\mathbf{B}/B$, respectively, and ε^{ijk} is the completely anti-symmetric unit tensor (Levi–Civita symbol).

Introducing the relativistic factor γ, cyclotron frequency ω_c, parallel velocity $v_\parallel$ and magnetic moment μ

$$\gamma=\sqrt{1+\frac{p^2}{m_0^2 c^2}}, \quad \omega_c=\frac{eB}{m_0 c \gamma},$$

$$v_\parallel=\frac{\lambda p}{m_0 \gamma}, \quad \mu=\frac{p^2(1-\lambda^2)}{2m_0 B}, \tag{5}$$

where m_0 is the mass of a particle at rest, the system governing the dynamics of drift particle motion in stationary electric and magnetic fields becomes

$$\frac{d}{dt}x^i=\frac{d}{dt}z^i=V^i(\mathbf{z})=v_g^i, \quad i=1...3, \tag{6}$$

$$\frac{d}{dt}p=\frac{d}{dt}z^4=V^4(\mathbf{z})=-em_0\frac{\gamma}{p}v_g^i\frac{\partial\Phi}{\partial x^i}, \tag{7}$$

$$\frac{d}{dt}\lambda=\frac{d}{dt}z^5=V^5(\mathbf{z})$$

$$=-\frac{1-\lambda^2}{\lambda}\left(em_0\frac{\gamma}{p^2}v_g^i\frac{\partial\Phi}{\partial x^i}+\frac{1}{2}v_g^i\frac{\partial\ln B}{\partial x^i}\right), \tag{8}$$

$$\frac{d}{dt}t=\frac{d}{dt}z^6=V^6(\mathbf{z})=1, \tag{9}$$

with the contravariant guiding center velocity v_g^i

$$v_g^i=\frac{1}{B_\parallel^*}\left(v_\parallel B^{*i}+\varepsilon^{ijk}\frac{cB_j}{B\sqrt{g}}\left(\frac{\partial\Phi}{\partial x^k}+\frac{\mu}{e\gamma}\frac{\partial B}{\partial x^k}\right)\right). \tag{10}$$

Here, Φ is the electrostatic potential and $v_\parallel$ as well as μ are to be expressed through p and λ using (5).

B. Stochastic mapping

Equation (1) describes both particle drift motion and velocity space diffusion as a single continuous process of particle motion along a stochastic orbit. In the long-mean-free-path regime, the velocity space diffusion and inelastic processes described by the right-hand side of (1) produce only a small change in the distribution function during the "bounce" time, which is defined as the time a particle needs to cross the characteristic magnetic field scale during the drift motion described by the left-hand side of (1). Due to this fact, one can discretize stochastic orbits with respect to one of the phase space variables. For this purpose, Poincaré cuts are introduced. These Poincaré cuts are five-dimensional hyper-surfaces in the six-dimensional phase-time space of the variables $\mathbf{z}$. For such hyper-surfaces it is required that each possible drift orbit intersects with at least one of those Poincaré cuts. Within the small Larmor radius approximation, the most convenient choice for these cuts are surfaces where the magnetic field has a local minimum along the magnetic-field line

$$\mathbf{h}(\mathbf{r})\cdot\nabla B(\mathbf{r})=h^i(\mathbf{x})\frac{\partial B(\mathbf{x})}{\partial x^i}=0, \tag{11}$$

where $\mathbf{h}=\mathbf{B}/B$ is the unit vector along the magnetic field. Usually, several such surfaces are present in a stellarator. The topology of these surfaces can be rather complex, and they have to be subdivided into a few regions with simpler topology. A convenient numbering of these regions in stellarators can be performed with the help of a two-dimensional (2D) vector index $\mathbf{m}=(n,m)$, where n numbers magnetic-field periods and m numbers the cuts within a single period.

From the set of the phase space variables $\mathbf{z}$ one can separate one spatial variable, e.g., x^3, which is monotonically increasing along the magnetic-field line. A convenient choice is the toroidal angle, $x^3=\varphi$. The remaining set of five variables is notated as $\mathbf{u}$ where

$$u^1=z^1=x^1, \quad u^2=z^2=x^2, \quad u^3=z^4=p,$$

$$u^4=z^5=\lambda, \quad u^5=z^6=t. \tag{12}$$

Equation (11) imposes no restrictions on the momentum space variables $u^3=p$ and $u^4=\lambda$ and on the time variable $u^5=t$. With respect to these variables the cuts have the same extent as the whole phase-time space $\mathbf{z}$. Together with the cut index $\mathbf{m}$, this set of variables, u^i, describes the positions of the footprints of the stochastic orbit on the Poincaré cuts, $(\mathbf{m},\mathbf{u})$. Without collisions, each new footprint of a drift orbit, $(\mathbf{m}',\mathbf{u}')$, is determined by the Poincaré map,

$$\mathbf{m}'=\mathbf{M}_\mathbf{m}(\mathbf{u}), \quad u'^i=U_\mathbf{m}^i(\mathbf{u}), \tag{13}$$

where $\mathbf{M}_\mathbf{m}(\mathbf{u})$ gives the index of the next cut to be passed by the drift orbit. This can be one of two neighboring cuts, then such particle is called "passing," or it can be the same cut for a "trapped" particle. The mapping function $U_\mathbf{m}^i(\mathbf{u})$ gives the coordinates on this next cut. This map is a regular map, because it is completely determined by the solution of the equations of particle drift motion (6)–(9) through $U_\mathbf{m}^i(\mathbf{u})$ $=Z^i(\mathbf{z}_\mathbf{m},\tau_{b\mathbf{m}})$ for $i=1,2$ and $U_\mathbf{m}^i(\mathbf{u})=Z^{i+1}(\mathbf{z}_\mathbf{m},\tau_{b\mathbf{m}})$ for $i=3...5$, where

$$\frac{\partial}{\partial\tau}Z^i(\mathbf{z},\tau)=V^i(\mathbf{Z}(\mathbf{z},\tau)), \quad Z^i(\mathbf{z},0)=z^i. \tag{14}$$

The coordinates of the starting point, $z_\mathbf{m}^i$ for $i\neq3$, are defined by (12) and $z_\mathbf{m}^3=x_\mathbf{m}^3$ is given by the solution of (11) for fixed x^1 and x^2

$$x_\mathbf{m}^3-\vartheta_\mathbf{m}(\mathbf{u})\equiv\Phi_\mathbf{m}(\mathbf{z}_\mathbf{m})=0, \tag{15}$$

where the starting point is on the cut $\mathbf{m}$. So, Eq. (15) is the same as (11) just resolved with respect to x^3 and $\Phi_\mathbf{m}$ defines the hyper-surface. Here, the full set of variables $\mathbf{u}$ is used in $\vartheta_\mathbf{m}(\mathbf{u})$ rather then x^1 and x^2 only, because in a more general case, the cut surface in coordinate space is not necessarily a minimum-B surface but could be a function of momentum space variables as well. This would be the case if, e.g., a parallel electrostatic field would be present. In particular, the map over the time variable is rather simple, $U_\mathbf{m}^5(\mathbf{u})=u^5$ $+\tau_{b\mathbf{m}}$, where $\tau_{b\mathbf{m}}=\tau_{b\mathbf{m}}(\mathbf{u})$ is a "bounce" time, which is the time needed for a particle transition from the cut $\mathbf{m}$ to the cut
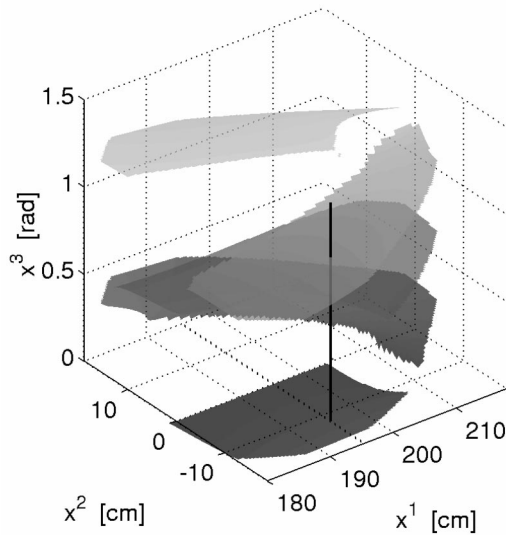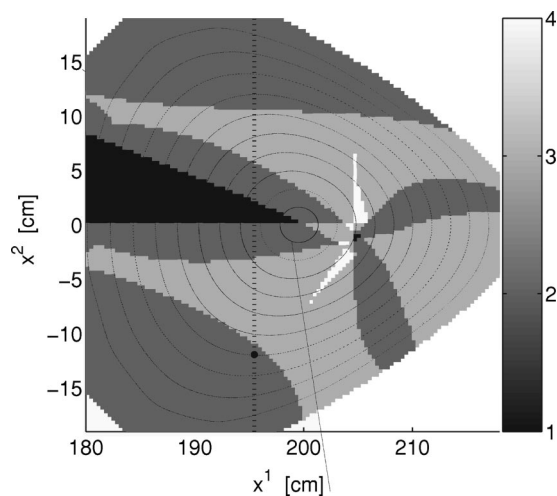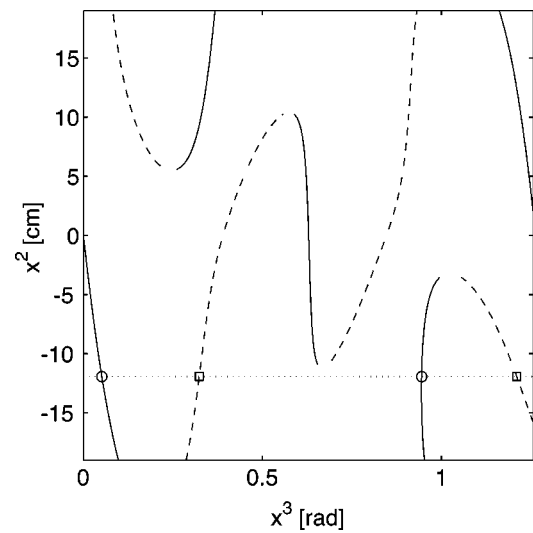
Phys. Plasmas, Vol. 9, No. 8, August 2002

Mapping technique for stellarators   3511

FIG. 1. The geometry of minimum-B cuts in W7-AS.

FIG. 3. Location of local minima (solid) and local maxima (dashed) reached along x^3 as a function of x^2.

$\mathbf{m}'$. Thus, particle motion is discretized with respect to the variable x^3 which is replaced by the cut index $\mathbf{m}$.
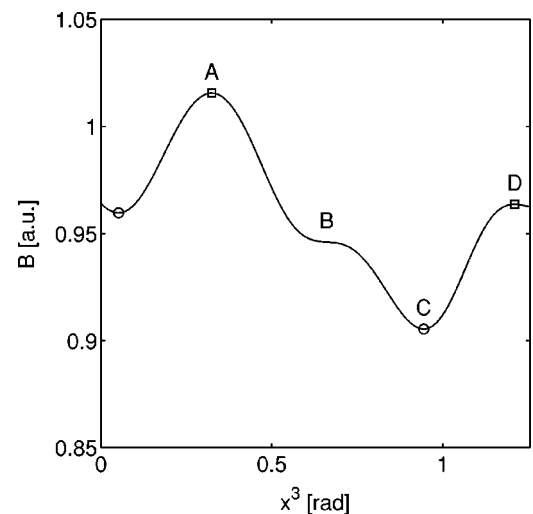
Figure 1 shows the spatial location of the Poincaré cuts within a field period for a real space configuration of stellarator W7-AS.[10] One can see, e.g., that along a specific magnetic-field line (vertical line), there exist two Poincaré cuts labeled with two specific values of the cut index m. The information about the transition between these cuts is contained in the discrete component of the Poincaré map (13). Starting from this point, a specific local magnetic coordinate system is used, such that the coordinates x^1 and x^2 stay unchanged along the magnetic field line. This kind of coordinate system is discussed in Sec. III A. Figure 2 shows the number of cuts as a function of x^1 and x^2. In this configuration, the number of cuts is in the range of 1–4. The dashed line at $x^1 = 195$ cm indicates the starting position for scans over x^2 of local minima and maxima reached along x^3 (along the magnetic field line). They are presented in Fig. 3. Here

again, the dashed line marks the field line where the modulus of B is presented as a function of x^3 in Fig. 4. Circles mark local minima and squares mark local maxima.

The cuts have a nontrivial topology. This requires a specific organization of storage of orbit information. The topology of cuts in the quasi-helically-symmetric configuration QHS[11] is less complicated (see Fig. 5) and is very close to the topology of a straight stellarator. Note that there exists a region where the number of cuts (Fig. 6) locally is zero. Through this region, passing orbits are mapped between cuts located in neighboring magnetic field periods. For details see Sec. III A.

In the presence of weak collisions and quasi-linear diffusion characterized by time scales $\tau_c \gg \tau_{b\mathbf{m}}$ or $\tau_{QL} \gg \tau_{b\mathbf{m}}$, respectively, the map has to include a small random perturbation of the particle coordinates $\delta u^i_{\mathbf{m}}(\mathbf{u})$ which describes the effect of these diffusive processes

FIG. 2. Number of cuts along the magnetic-field line within one magnetic-field period as function of local magnetic coordinates x^1 and x^2 for W7-AS.

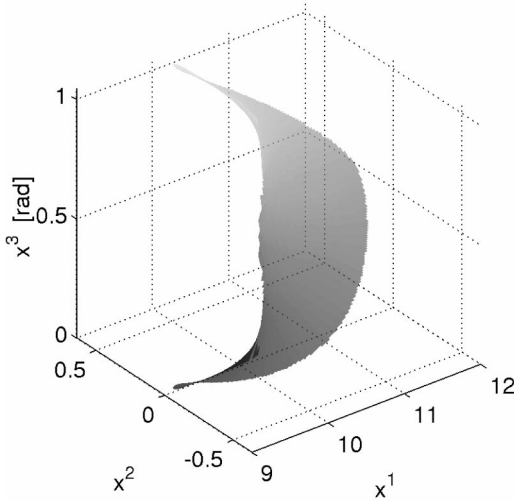FIG. 4. Modulus of B vs x^3 along the dotted field line in Fig. 3.

FIG. 5. The geometry of minimum-B cuts in QHS.

$$\mathbf{m}' = \mathbf{M_m}(\mathbf{u} + \delta\mathbf{u_m}(\mathbf{u})) \equiv \tilde{\mathbf{M}}_\mathbf{m}(\mathbf{u}),$$

$$u'^i = U^i_\mathbf{m}(\mathbf{u} + \delta\mathbf{u_m}(\mathbf{u})) \equiv \tilde{U}^i_\mathbf{m}(\mathbf{u}). \qquad (16)$$

Therefore, such a mapping becomes stochastic. The random perturbations entering the stochastic map (16) have been obtained from the drift-kinetic equation in Ref. 5. Also in this reference, the drift kinetic equation has been transformed to an integral equation describing the conservation of the pseudo-scalar particle flux density $\Gamma_\mathbf{m}$ through the Poincaré cuts. Following the lines of Ref. 5 (see Appendix A), this equation can be written in the following form:

$$\Gamma_{\mathbf{m}'}(\mathbf{u}') = \sum_\mathbf{m} \int d^5u \langle \delta_{\mathbf{m}', \tilde{\mathbf{M}}_\mathbf{m}(\mathbf{u})} \delta(\mathbf{u}' - \tilde{\mathbf{U}}_\mathbf{m}(\mathbf{u})) \rangle$$

$$\times (1 - \bar{\nu}_\mathbf{m}(\mathbf{u}))(\Gamma_\mathbf{m}(\mathbf{u}) + \mathcal{Q}_\mathbf{m}(\mathbf{u})). \qquad (17)$$

Here $\Gamma_\mathbf{m} = dN/2\pi d^5u = J_\mathbf{m}f$, where dN is the number of particles passing through the element of the cut area $du^1 du^2 du^3 du^4 = dx^1 dx^2 dp\, d\lambda$ in coordinate and in momentum space during the time $dt = du^5$ due to their drift motion. This quantity is proportional to the distribution function f
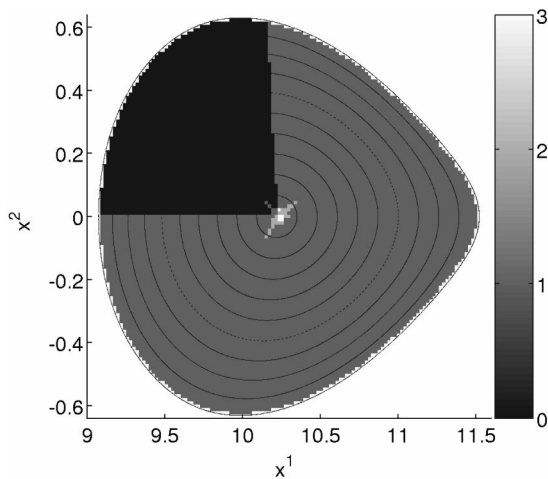

FIG. 6. The same as Fig. 2 for QHS.

where the Jacobian $J_\mathbf{m}$ is expressed through the normal component of the six-dimensional velocity (6)–(9) with respect to the Poincaré cut

$$J_\mathbf{m}(\mathbf{u}) = \frac{V^i(\mathbf{z_m})dS_i}{du^1 \cdots du^5} = J(\mathbf{z})V^i(\mathbf{z}) \left.\frac{\partial \Phi_\mathbf{m}(\mathbf{z})}{\partial z^i}\right|_{\mathbf{z} = \mathbf{z_m}}, \qquad (18)$$

where dS_i is the element of the hyper-surface. The explicit expression for $J_\mathbf{m}$ is given in Appendix B. The other quantities in (17)

$$\bar{\nu}_\mathbf{m}(\mathbf{u}) = \int_0^{\tau_{b\mathbf{m}}} d\tau\, \nu(\mathbf{Z}(\mathbf{z_m},\tau)),$$

$$\mathcal{Q}_\mathbf{m}(\mathbf{u}) = J_\mathbf{m}\bar{Q}_\mathbf{m}(\mathbf{u}), \qquad (19)$$

$$\bar{Q}_\mathbf{m}(\mathbf{u}) = \int_0^{\tau_{b\mathbf{m}}} d\tau\, Q(\mathbf{Z}(\mathbf{z_m},\tau)),$$

are the orbit integrated sink rate ($\bar{\nu}_\mathbf{m} \ll 1$) and the orbit integrated source, respectively, and $\delta(\mathbf{u} - \tilde{\mathbf{U}}_\mathbf{m}) = \delta(u^1 - \tilde{U}^1_\mathbf{m}) \cdots \delta(u^5 - \tilde{U}^5_\mathbf{m})$. Angular brackets $\langle \cdots \rangle$ denote the average over random perturbations δu^i which satisfy

$$\langle \delta u^i \rangle = \mathcal{F}^{i'}_\mathbf{m}, \quad \langle \delta u^i \delta u^j \rangle = 2\bar{D}^{i'j'}_\mathbf{m}, \qquad (20)$$

where $i' = i$ and $j' = j$ for i, $j \leq 2$ and $i' = i+1$ and $j' = j+1$ for i, $j > 2$. Note that in the long-mean-free-path regime, the higher order moments of the random perturbations δu^i produce higher order corrections to the approximate equation (17) over the small parameter $\tau_{b\mathbf{m}}/\tau_c$, and, therefore, are not important. This leaves a significant freedom in the definition of δu^i. A particular form of δu^i convenient for Monte Carlo modeling is

$$\delta u^i = \sqrt{2}\alpha^{ij}_\mathbf{m}\xi_j + \mathcal{F}_\mathbf{m}, \qquad (21)$$

where the matrix $\alpha^{ij}_\mathbf{m}$ satisfies

$$\alpha^{ik}_\mathbf{m}\alpha^{jl}_\mathbf{m}\delta_{kl} = \bar{D}^{ij}_\mathbf{m}, \qquad (22)$$

and ξ_i is the set of independent standard random numbers satisfying the relations

$$\langle \xi_i \rangle = 0, \quad \langle \xi_i \xi_j \rangle = \delta_{ij}, \qquad (23)$$

where δ_{ij} is the Kronecker symbol. The orbit integrated diffusion operator coefficients in (20) are given by

$$\mathcal{F}^i_\mathbf{m} = \bar{F}^i_\mathbf{m} + \frac{1}{J_\mathbf{m}}\frac{\partial}{\partial u^j} J_\mathbf{m}\bar{D}^{ij}_\mathbf{m}, \qquad (24)$$

$$\bar{F}^i_\mathbf{m} = \int_0^{\tau_{b\mathbf{m}}} d\tau\, \bar{c}^i_k(\tau)F^k(\mathbf{Z}(\mathbf{z_m},\tau)),$$

$$\bar{D}^{ij}_\mathbf{m} = \int_0^{\tau_{b\mathbf{m}}} d\tau\, \bar{c}^i_k(\tau)\bar{c}^j_l(\tau)D^{kl}(\mathbf{Z}(\mathbf{z_m},\tau)), \qquad (25)$$

where $\bar{c}^i_k$ is the transformation matrix from the local coordinates on the trajectory, $\mathbf{Z}(\mathbf{z_m},\tau)$, to Lagrangian coordinates $\mathbf{z}_L$ (coordinates of the trajectory starting point on the Poincaré cut $\mathbf{u}$ and trajectory parameter τ; see Appendix A). This matrix satisfies the equation set

$$\frac{\partial}{\partial \tau}\bar{c}_k^i(\tau) = -\bar{c}_l^i(\tau)\frac{\partial V^l(\mathbf{z}')}{\partial z'^k}\bigg|_{\mathbf{z}' = \mathbf{Z}(\mathbf{z_m},\tau)}, \tag{26}$$

and the initial conditions on the cut (equation for $i=3$ is not used)

$$\bar{c}_k^i(0) = \delta_k^i - V^i(\mathbf{z})\frac{\partial \Phi_\mathbf{m}(\mathbf{z})}{\partial z^k}\left(V^j(\mathbf{z})\frac{\partial \Phi_\mathbf{m}(\mathbf{z})}{\partial z^j}\right)^{-1}\bigg|_{\mathbf{z}=\mathbf{z_m}},$$

$$i \neq 3. \tag{27}$$

The solution of (17) is required mainly for the computation of various phase space–time integrals of the distribution function which take the form[5]

$$\int dt \int d^3p \int d^3r A(\mathbf{r},\mathbf{p},t)f(\mathbf{r},\mathbf{p},t)$$

$$= 2\pi \int d^6 z A(\mathbf{z}) = 2\pi \sum_\mathbf{m} \int d^5 u \Gamma_\mathbf{m}(\mathbf{u})\bar{A}_\mathbf{m}(\mathbf{u}). \tag{28}$$

This form of integrals is a straightforward result of the change of integration variables $\mathbf{z}$ to Lagrangian variables $\mathbf{z}_L$ introduced in Appendix A. If A is a function of gyro-phase ϕ, gyro-averaging is also implied in the expression for $\bar{A}_\mathbf{m}(\mathbf{u})$

$$\bar{A}_\mathbf{m}(\mathbf{u}) = \frac{1}{2\pi}\int_0^{\tau_{b\mathbf{m}}} d\tau \int_{-\pi}^{\pi} d\phi A(\mathbf{Z}(\mathbf{z_m},\tau),\phi). \tag{29}$$

Practically, it is not necessary to use the exact orbit in (29) in the majority of cases. It is sufficient to replace $\mathbf{Z}(\mathbf{z_m},\tau)$ with a simplified orbit containing only the parallel motion. In more details, the assumptions used for the computation of averages are described in Appendix C.

C. Monte Carlo algorithm

The integral equation (17) is of the type of a second kind Fredholm integral equation which can be solved with a standard Monte Carlo method. For this purpose the equation is written in the following operator form:

$$\Gamma_\mathbf{m}(\mathbf{u}) = \hat{K}(\Gamma_\mathbf{m}(\mathbf{u}) + \mathcal{Q}_\mathbf{m}(\mathbf{u})), \tag{30}$$

where $\hat{K}$ denotes the integral-sum operation

$$\hat{K}A_{\mathbf{m}'}(\mathbf{u}') \equiv \sum_\mathbf{m} \int d^5 u K_{\mathbf{m}',\mathbf{m}}(\mathbf{u}',\mathbf{u})A_\mathbf{m}(\mathbf{u}), \tag{31}$$

$$K_{\mathbf{m}',\mathbf{m}}(\mathbf{u}',\mathbf{u}) = M_{\mathbf{m}',\mathbf{m}}(\mathbf{u}',\mathbf{u})(1-\bar{\nu}_\mathbf{m}(\mathbf{u})), \tag{32}$$

$$M_{\mathbf{m}',\mathbf{m}}(\mathbf{u}',\mathbf{u}) = \langle \delta_{\mathbf{m}',\tilde{M}_\mathbf{m}(\mathbf{u})}\delta(\mathbf{u}'-\tilde{U}_\mathbf{m}(\mathbf{u}))\rangle. \tag{33}$$

The formal solution to (30) is given through the series

$$\Gamma_\mathbf{m}(\mathbf{u}) = \sum_{k=1}^{\infty} \hat{K}^k \mathcal{Q}_\mathbf{m}(\mathbf{u}). \tag{34}$$

In order to construct the statistical estimate of the solution, one introduces test particles characterized by their position $(\mathbf{m},\mathbf{u})$ and by their statistical weight w. Then, a Markov chain is the sequence of particle positions and weights $(\mathbf{m}_k, \mathbf{u}_k, w_k)$ where $k=0,1,2\ldots$. Each new position and weight $(\mathbf{m}_{k+1}, \mathbf{u}_{k+1}, w_{k+1})$ are determined from the previous ones

by the stochastic map (16) with $(\mathbf{m},\mathbf{u})=(\mathbf{m}_k,\mathbf{u}_k)$ and $(\mathbf{m}_{k+1},\mathbf{u}_{k+1})=(\mathbf{m}',\mathbf{u}')$ [function (33) is the probability distribution function for this transition] and by sampling the weight

$$w_{k+1} = W_\mathbf{m}(\mathbf{u}_k,w_k),$$

$$\langle W_\mathbf{m}(\mathbf{u}_k,w_k)\rangle = (1-\bar{\nu}_\mathbf{m}(\mathbf{u}))w_k. \tag{35}$$

This is realized by putting w_{k+1} to w_k with the probability $(1-\bar{\nu}_\mathbf{m}(\mathbf{u}))$ and putting it to zero otherwise. In the second case, the Markov chain is terminated. Presenting the source $\mathcal{Q}_\mathbf{m}(\mathbf{u})$ as

$$\mathcal{Q}_\mathbf{m}(\mathbf{u}) = w_0 P_\mathbf{m}^{(Q)}(\mathbf{u}), \quad P_\mathbf{m}^{(Q)}(\mathbf{u})>0,$$

$$\sum_\mathbf{m} \int d^5 u P_\mathbf{m}^{(Q)}(\mathbf{u}) = 1, \tag{36}$$

where the initial weight w_0 with $|w_0|=$ const satisfies sign$(w_0)=$ sign$(\mathcal{Q}_\mathbf{m}(\mathbf{u}))$ the initial point of the Markov chain $(\mathbf{m}_0, \mathbf{u}_0)$ is chosen randomly so that

$$\langle \delta_{\mathbf{m},\mathbf{m}_0}\delta(\mathbf{u}-\mathbf{u}_0)\rangle = P_\mathbf{m}^{(Q)}(\mathbf{u}), \tag{37}$$

e.g., the rejection technique (see, e.g., Ref. 15) can be used for this purpose. Thus, the formal solution (34) is given by an average over Markov chains

$$\Gamma_\mathbf{m}(\mathbf{u}) = \left\langle \sum_{k=1}^{\infty} w_k \delta_{\mathbf{m},\mathbf{m}_k}\delta(\mathbf{u}-\mathbf{u}_k)\right\rangle. \tag{38}$$

Practically, instead of $\Gamma_\mathbf{m}(\mathbf{u})$ various phase–time space integrals of this quantity are computed within the Monte Carlo procedure

$$2\pi \cdot \sum_\mathbf{m} \int d^5 u \Gamma_\mathbf{m}(\mathbf{u})\bar{A}_\mathbf{m}(\mathbf{u}) = 2\pi \left\langle \sum_{k=1}^{\infty} w_k \bar{A}_{\mathbf{m}_k}(\mathbf{u}_k)\right\rangle. \tag{39}$$

In particular, the flux density $\Gamma_{\mathbf{m}'}(\mathbf{u}')$ is also approximated by such an integral with $\bar{A}_\mathbf{m}(\mathbf{u}) = 1/(\Delta u^1 \cdots \Delta u^5)$ for $\mathbf{m}=\mathbf{m}'$, $u'^i - \Delta u^i/2 < u^i < u'^i + \Delta u^i/2$ and $\bar{A}_\mathbf{m}(\mathbf{u})=0$ otherwise.

Note that the Monte Carlo procedure described above contains as a particular case the conventional MC procedure[1] if instead of the minimum-B cuts one uses the cuts $t=t_m \equiv t_0 + m\Delta t$ where Δt is the time integration step of the equation of drift particle motion and $m=1,2,3,\ldots$ is the number of the integration step. In this case the regular map $U_\mathbf{m}^i(\mathbf{u})$ is obtained using a step integration method (e.g., Runge–Kutta) instead of using the interpolation of the stored map as it is done in the present paper.

III. MAPPING IN STELLARATOR GEOMETRY

A. Local magnetic coordinate systems

In a general magnetic field topology, the particle motion can conveniently be described using a set of local magnetic coordinates $\mathbf{x}$ instead of a unique coordinate system for the whole plasma volume. For such coordinates, the requirement is that two of these coordinates satisfy the magnetic differential equation

$$\mathbf{h} \cdot \nabla x^i = 0, \quad i = 1,2. \tag{40}$$

In such coordinate systems the fast parallel motion leaves the coordinates x^1 and x^2 unchanged while the small cross-field particle displacements due to the drift during the "bounce" period are directly given by increments of these coordinates, Δx^1 and Δx^2. Therefore, relatively large relative errors in Δx^1 and Δx^2 do not introduce significant numerical cross-field transport. This is a positive feature which is not easily realized in real-space coordinates. Therefore, such a coordinate system allows to reduce the computer memory necessary for the storage of particle orbit data which in turn is needed for the orbit reconstruction.

In a general magnetic field, two families of linearly independent single-valued solutions to the magnetic differential equation (40) do not exist unless the magnetic-field lines are closed (closed at infinity, in particular). In a special case with existing magnetic surfaces, (40) has only one family of such solutions. These are surfaces of constant magnetic flux, a quantity which is used as one of the coordinates in a flux coordinate system. Therefore, in order to use the solutions of the magnetic differential equation (40) as coordinates in the general case, it is necessary to introduce a surface which cuts the magnetic-field lines. This cut is called "reference cut" and serves as a periodic boundary separating the regions where the functions x^1 and x^2 are single valued. For toroidal magnetic field configurations, this can be a toroidal cut, $\varphi = \text{const}$, where φ is the azimuth (toroidal angle) of the cylindrical coordinate system (R,Z,φ), and R and Z are the radius counted from the main axis of the torus and the distance along the main axis of the torus, respectively. For stellarators, it is more convenient to introduce several reference cuts,

$$\varphi = \varphi_n, \quad \varphi_n = \frac{2\pi n}{N},$$

$$n = 0, \ldots, N-1, \tag{41}$$

where N is the number of toroidal stellarator magnetic field periods. In this way N local magnetic coordinate systems (LMCS), each associated with its own cut, are introduced. Since the domains of coordinate systems, $\varphi_n < \varphi < \varphi_n + 2\pi$, overlap, the particle position can be uniquely described in a few coordinate systems simultaneously (Multiple Coordinate System Approach[6]) by the cut index, n, and the set of local magnetic coordinates (x^1, x^2, x^3) associated with this cut. The parallel variable is given as

$$x^3 \equiv \varphi - \varphi_n, \tag{42}$$

and the local magnetic coordinates x^1 and x^2 are defined, respectively, as cylindrical coordinates R' and Z' of the projection along the field line of the particle position (R,Z,φ) to the reference cut $\varphi = \varphi_n$. Formally, this is done with help of the characteristics of the magnetic differential equation (40), functions $X^1(R,Z,\varphi;\varphi')$ and $X^2(R,Z,\varphi;\varphi')$, as follows:

$$x^i \equiv X^i(R,Z,\varphi;\varphi_n), \quad i = 1,2. \tag{43}$$

Functions X^1 and X^2 satisfy the magnetic-field line equations

$$\frac{\partial X^1}{\partial \varphi'} = \frac{h^R(X^1,X^2,\varphi')}{h^\varphi(X^1,X^2,\varphi')},$$

$$\frac{\partial X^1}{\partial \varphi'} = \frac{h^Z(X^1,X^2,\varphi')}{h^\varphi(X^1,X^2,\varphi')}, \tag{44}$$

and the initial conditions

$$X^1(R,Z,\varphi;\varphi) = R, \quad X^2(R,Z,\varphi;\varphi) = Z. \tag{45}$$

Here $h^R(R,Z,\varphi)$, $h^\varphi(R,Z,\varphi)$ and $h^Z(R,Z,\varphi)$ are the contravariant components of $\mathbf{h}$ in the cylindrical coordinate system. Equation (40) can be checked using the group property of characteristics,

$$X^i(X^1(R,Z,\varphi;\varphi''),X^2(R,Z,\varphi;\varphi''),\varphi'';\varphi')$$
$$= X^i(R,Z,\varphi;\varphi'). \tag{46}$$

Taking the derivative of (46) with respect to φ'' and putting $\varphi'' = \varphi$ and $\varphi' = \varphi_n$ in the final expression with the help of (45) and (43), one obtains (40).

Multiple local coordinate systems permit to exploit the advantage of the Monte Carlo method to model particle motion in the most convenient coordinate system. The final position of a particle, which is needed for statistical accounting, is obtained by a (set of) coordinate transforms. For the purpose of statistical accounting, the "preferred" coordinate system domains are introduced as follows, $\varphi_n < \varphi < \varphi_{n+1}$. The link between the neighboring LMCS is obtained with the help of (46)

$$x^i_{(n\pm 1)} \equiv X^i(R,Z,\varphi;\varphi_{n\pm 1}) = X^i(x^1_{(n)},x^2_{(n)},\varphi_n;\varphi_{n\pm 1}),$$

$$i = 1,2; \quad x^3_{(n\pm 1)} = x^3_{(n)} \mp \frac{2\pi}{N}. \tag{47}$$

Here the subscript (n) has been introduced in order to distinguish between different LMCS. If stellarator symmetry exists and all magnetic-field periods are equivalent, such a variable change can be described by two sets of functions

$$x^i_{(n\pm 1)} = X^i_\pm(x^1_{(n)},x^2_{(n)}), \tag{48}$$

where

$$X^i_\pm(x^1,x^2) \equiv X^i\left(x^1,x^2,0;\pm\frac{2\pi}{N}\right), \tag{49}$$

defines the magnetic-field map in positive $(+)$ and negative $(-)$ directions, respectively. If stellarator symmetry is destroyed, the sets of mapping functions have to be defined for each period separately.

Since in local magnetic coordinates the slow cross-field motion is clearly separated from the fast parallel motion, the only source of cross-field numerical diffusion can arise from a coordinate change. Therefore, the mapping functions (49) are reconstructed numerically with high accuracy using a fine mesh of data points and bi-cubic splines for interpolation. Since these functions are two-dimensional, the requirement for computer memory stays within reasonable limits.

It should be mentioned that multiple LMCS place no restrictions on the topology of the magnetic field, thus allowing the treatment of island structures and ergodic magnetic field layers as well as regular magnetic surfaces.[6] At the

same time, for configurations with embedded magnetic surfaces only, where Boozer coordinates (ψ, θ, φ) can be established, the definition of LMCS is trivial

$$x^1 = \psi, \quad x^2 = \theta - \iota(\varphi - \varphi_n),$$

$$x^3 = \varphi - \varphi_n. \tag{50}$$

Here $\iota = \iota(\psi)$ is the rotational transform angle in units of 2π, ψ is a flux label and θ is a poloidal angle. The magnetic-field map (49) is also simplified,

$$X^1_\pm(x^1, x^2) \equiv x^1,$$

$$X^2_\pm(x^1, x^2) \equiv x^2 \pm \iota(x^1) \frac{2\pi}{N}. \tag{51}$$

With the help of multiple local magnetic coordinate systems, the numbering of minimum-B cuts is performed with two indices, $(n, m) \equiv \mathbf{m}$, where n is the index of the "preferred" domain of LMCS (magnetic-field period) and m is the index of the minimum-B surface region within this period. For unambiguous indexing, these surfaces are split into regions in such a way that no magnetic-field line intersects such a surface twice within a magnetic-field period. To ensure this, the same minimum-B surface has, if necessary, to be split into a few regions within the field period. It is also split into different "cuts" by the reference cut if the given surface extends through the chosen boundary of the magnetic field period.

B. Poincaré mapping in small Larmor radius approximation

The unperturbed map $U^i_{\mathbf{m}}(\mathbf{u})$ can be constructed now in LMCS containing the starting point within its preferred domain. If the end point belongs to the same preferred domain the spatial components of the Poincaré map (13) can be written as

$$U^{1,2}_{\mathbf{m}}(\mathbf{u}) = u^{1,2} + \Delta x^{1,2}_{\mathbf{m}}(\mathbf{u}), \tag{52}$$

where $\Delta x^{1,2}_{\mathbf{m}}$ are displacements of the footprint. As it will be seen below, these displacements which describe the effects of the magnetic and electric drift can be expanded in a series over the Larmor radius. If the end point belongs to the "preferred domain" of a different LMCS, coordinates (52) must be transformed using the magnetic-field mapping (48) or a series of such transforms if a particle travels through more than one magnetic-field period during its bounce time.

The momentum space components of the Poincaré map, $U^3_{\mathbf{m}}(\mathbf{u})$ and $U^4_{\mathbf{m}}(\mathbf{u})$, can be obtained using the conservation of the magnetic moment (5) and of the total energy $w = m_0 c^2 \gamma + e\Phi$.

In the following it is assumed that the electrostatic potential Φ is constant along the magnetic field, $\Phi = \Phi(\psi)$ where $\psi = \psi(x^1, x^2)$ is the flux surface label, and that energies of particles are nonrelativistic, $p^2 \ll m_0^2 c^2$. In this case, one can introduce three scaling parameters for Δx^i and present Δx^i in the form of the expansion over these parameters. First, the normalized time τ, the dimensionless mo-

mentum $\hat{p}$, the dimensionless magnetic field $\hat{B}$, and the dimensionless electrostatic potential $\hat{\Phi}$ are introduced according to

$$\tau = \frac{p_0 t}{m_0}, \quad \hat{p} = \frac{p}{p_0},$$

$$\hat{B} = \frac{B}{B_0}, \quad \hat{\Phi} = \frac{e\Phi}{T}, \tag{53}$$

respectively, where p_0 is the starting value of particle momentum, B_0 is a reference magnetic field, and T is the plasma temperature. Here $\hat{\Phi} \sim 1$ is assumed. Introducing also the normalized magnetic and electric drift velocities $\hat{v}^i_B$ and $\hat{v}^i_E$ according to

$$\hat{v}^i_B \equiv \frac{\hat{p}^2}{2\hat{B}\sqrt{g}} \left[2\lambda^2 (\varepsilon^{ijk} - h^i h_l \varepsilon^{ljk}) \frac{\partial h_k}{\partial x^j} \right.$$

$$\left. + (1 - \lambda^2) \varepsilon^{ijk} h_j \frac{\partial \log \hat{B}}{\partial x^k} \right], \tag{54}$$

$$\hat{v}^i_E \equiv \frac{\hat{p}^2}{2\hat{B}\sqrt{g}} \varepsilon^{ijk} h_j \frac{\partial \psi}{\partial x^k}, \tag{55}$$

respectively, the equations of motion (6)–(8) are transformed to

$$\frac{dx^i}{d\tau} = \rho_B \hat{v}^i_B + a_E \hat{v}^i_E, \quad i = 1, 2, \tag{56}$$

$$\frac{dx^3}{d\tau} = \hat{p}\lambda h^3, \tag{57}$$

$$\frac{d\hat{p}}{d\tau} = -\frac{a_E}{2\hat{p}} \hat{v}^i_B \frac{\partial \psi}{\partial x^i}, \tag{58}$$

$$\frac{d\lambda}{d\tau} = \frac{1 - \lambda^2}{\lambda} \left(\frac{1}{\hat{p}} \frac{d\hat{p}}{d\tau} - \frac{1}{2} \hat{v}^i_B \frac{\partial \log \hat{B}}{\partial x^i} \right), \tag{59}$$

where

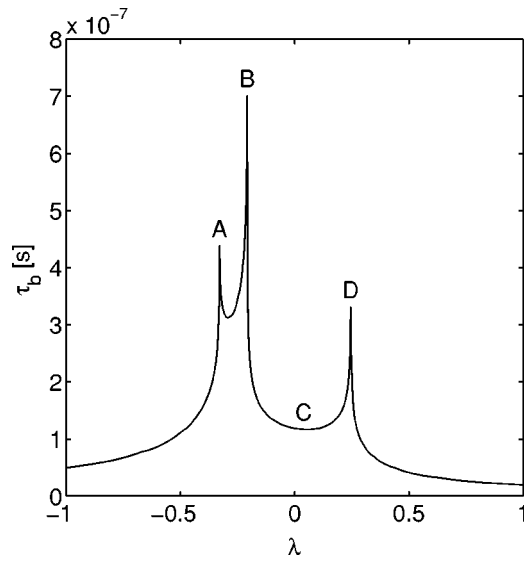$$a_E = \frac{\rho_0}{\bar{p}_0} \frac{d\Phi}{d\psi} \approx \rho_E + \rho_{EE}(\psi - \psi_0). \tag{60}$$

Here

$$\rho_B = \rho_0 \bar{p}_0, \quad \rho_E = \frac{\rho_0}{\bar{p}_0} \frac{d\hat{\Phi}(\psi_0)}{d\psi_0},$$

$$\rho_{EE} = \frac{\rho_0}{\bar{p}_0} \frac{d^2\hat{\Phi}(\psi_0)}{d\psi_0^2}, \tag{61}$$

$$\bar{p}_0 = \frac{p_0}{\sqrt{2m_0 T}}, \quad \rho_0 = \frac{1}{\omega_{c0}} \sqrt{\frac{2T}{m_0}},$$

$$\omega_{c0} = \frac{eB_0}{m_0 c}, \tag{62}$$

and ψ_0 is a starting value of the flux surface label. The solution to (56)–(59) is obtained using starting conditions $\hat{p}$

FIG. 7. "Bounce"-time $\tau_{b\mathbf{m}}$ vs particle pitch λ for the minimum C in Fig. 6.

FIG. 8. Displacement of particles, $\Delta x_{\mathbf{m}}^i$, vs particle pitch λ without radial electric field.

$=1$ and $\psi=\psi_0$. Defining the normalized bounce time which is independent from p_0 in the zero-order Larmor radius expansion as $\hat{\tau}_{b\mathbf{m}}=\tau_{b\mathbf{m}}p_0/m_0$, the displacements Δx^i are obtained as
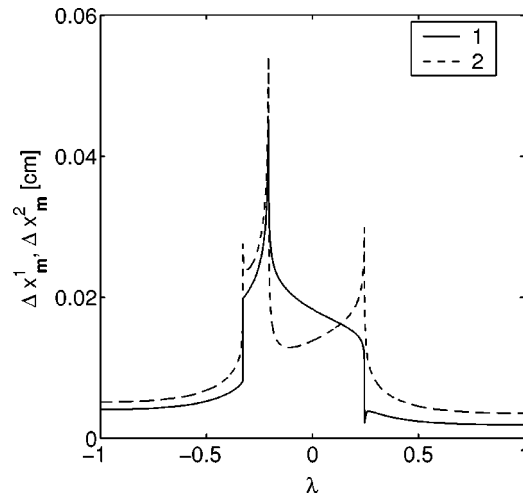
$$\Delta x_{\mathbf{m}}^i \equiv x^i|_{\hat{\tau}=\hat{\tau}_{b\mathbf{m}}}-x^i|_{\hat{\tau}=0}. \tag{63}$$

Since all three parameters (61) are proportional to the Larmor radius ρ_0, the displacements are presented in the form of a Taylor series up to second order terms in ρ_0

$$\Delta x_{\mathbf{m}}^i = \left(\frac{\partial \Delta x_{\mathbf{m}}^i}{\partial \rho_E}\right)_0 \rho_E + \left(\frac{\partial \Delta x_{\mathbf{m}}^i}{\partial \rho_B}\right)_0 \rho_B$$

$$+ \left(\frac{\partial^2 \Delta x_{\mathbf{m}}^i}{\partial \rho_B \partial \rho_{EE}}\right)_0 \rho_B \rho_{EE} + \frac{1}{2}\left(\frac{\partial^2 \Delta x_{\mathbf{m}}^i}{\partial \rho_B^2}\right)_0 \rho_B^2$$

$$+ \left(\frac{\partial^2 \Delta x_{\mathbf{m}}^i}{\partial \rho_B \partial \rho_E}\right)_0 \rho_B \rho_E + \frac{1}{2}\left(\frac{\partial^2 \Delta x_{\mathbf{m}}^i}{\partial \rho_E^2}\right)_0 \rho_E^2, \tag{64}$$

where $(\cdots)_0$ denotes that the value for $\rho_B=\rho_E=\rho_{EE}=0$. Here, only nonzero terms are listed. The expansion coefficients are three-dimensional (3D) functions of x^1, x^2 and λ. Thus, usage of the local magnetic coordinates reduces the amount of necessary storage to amounts reasonable on modern workstations. Moreover, since the radial electric field profile enters only through the parameters ρ_E and ρ_{EE}, Eq. (64) allows for iterations with a varying electrostatic potential during an MC run without any need for reloading the maps. Note that one needs the knowledge of the flux label ψ only for the description of the effects of the radial electric field. If these effects are small, the assumption of existence of embedded magnetic surfaces is not necessary.

The dependence of the bounce time $\tau_{b\mathbf{m}}$ on the particle pitch λ is shown in Fig. 7 for a specific minimum denoted with C in Fig. 4. One can see the rather "rich" behavior including logarithmic singularities located at the two neigh-

boring maxima—A and D—and at the saddle-point marked with B. This behavior has to be handled by subdividing the interpolation range.

It should be mentioned that for small Larmor radii, the mapping procedure is equivalent to tracing the contours of the parallel adiabatic invariant[5] with deterministic transitions between different classes of trapped particles. In this approximation a re-scaling of the Larmor radius is allowed without consequences for the shape of the orbits. Actually, within the mapping procedure the Larmor radius and collision terms can be scaled with the same factor. This is demonstrated in Sec. IV D. Thus, even high energy ions or a very strong radial electric field can be treated by this approach as long as one assumes conservation of the parallel adiabatic invariant. As it is known, the transition between classes of particles are not deterministic as soon as one assumes the gyro-phase to be random before the transition. Nevertheless, in the present application to electrons, the presence of Coulomb collisions introduces an even higher uncertainty than collision-less transition probabilities. Therefore, the usage of deterministic transitions is fully justified.

The 3D interpolation of the coefficients in (64) is performed with quadratic polynomial interpolation on the equidistant grid in the coordinate space (x^1,x^2) and with a nonequidistant grid over the particle pitch λ. This grid is fitted to the behavior of the bounce time.

The reconstruction of particle displacements $\Delta x_{\mathbf{m}}^i$ with the help of the Taylor series (64) is shown in Figs. 8 and 9 for W7-AS without and with a radial electric field, respectively. Here, the reference magnetic field $B_0=25$ kG, the particle kinetic energy $w_k=8$ keV, and the radial electric field $E_r=393$ V/cm. The grid size in coordinate space is 120 times 120. The reconstruction of the pitch angle dependence is performed with 60 grid points in the trapped region and with 20 grid points in the passing region. This allows to keep the interpolation error below 1%. One can again see the strong influence of neighboring maxima and saddle-points. In the case with a radial electric field, one can also see that the displacement reflects the behavior of the bounce time in
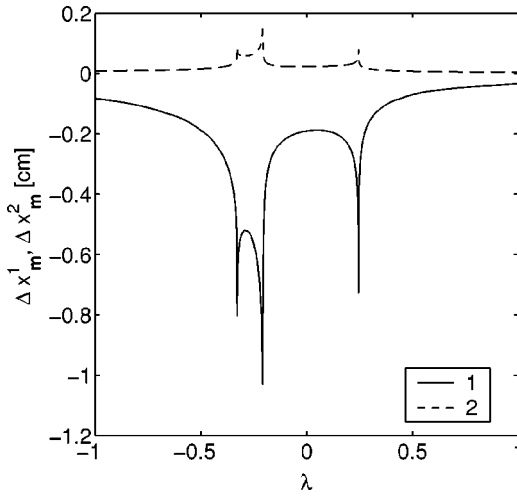
FIG. 9. Displacement of particles, $\Delta x_{\mathbf{m}}^i$, vs particle pitch λ with radial electric field.

Fig. 7 very well since the electric drift velocity does not depend on particle pitch.

In Fig. 10, the variance (20) of λ, $\langle \delta \lambda^2 \rangle$, after one bounce time is presented as function of λ. The exact form of the collision integral is discussed in Sec. III C. It has to be mentioned that only derivatives of this quantity show a singular behavior.

C. Coulomb collisions

In the present realization of the code, the effect of Coulomb collisions is taken into account in velocity space only and the spatial components of $\bar{D}_{\mathbf{m}}^{ij}$ and $\mathcal{F}_{\mathbf{m}}^i$ are neglected in the stochastic map. Therefore, only the strongest particle transport effects stemming from the magnetic-field asymmetry are correctly described. Assuming the scattering background plasma to be an isotropic Maxwellian, the local form of the collision integral is
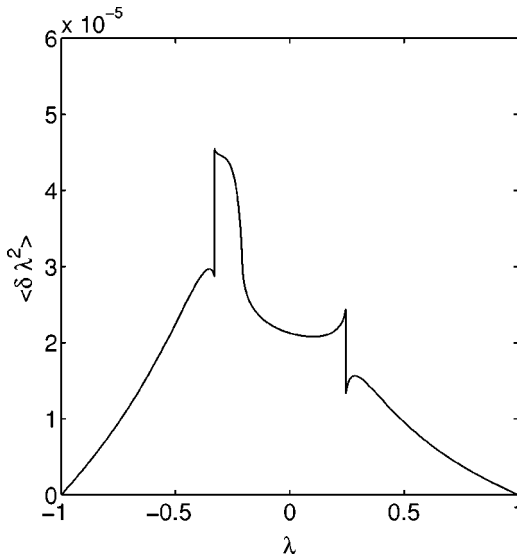
$$St(f) = \frac{1}{p^2} \frac{\partial}{\partial p} p^2 D_C^{pp}(p) \left(\frac{\partial f}{\partial p} + \frac{pf}{m_0 T} \right)$$

$$+ D_C^{\chi\chi}(p) \frac{\partial}{\partial \lambda} (1 - \lambda^2) \frac{\partial f}{\partial \lambda}. \tag{65}$$

Then, in zero-order approximation over the Larmor radius, there exist only three nonzero components of the orbit-integrated diffusion coefficients (25)

$$\bar{D}_{C\mathbf{m}}^{pp}(\mathbf{u}) = \frac{m_0}{p} D_C^{pp}(p) \hat{\tau}_{b\mathbf{m}}(x^1, x^2, \lambda), \tag{66}$$

$$\bar{D}_{C\mathbf{m}}^{\lambda\lambda}(\mathbf{u}) = \frac{m_0}{p} D_C^{\chi\chi}(p) \Lambda_{\mathbf{m}}(x^1, x^2, \lambda), \tag{67}$$

$$\bar{F}_{C\mathbf{m}}^p(\mathbf{u}) = -\frac{p}{m_0 T} \bar{D}_{C\mathbf{m}}^{pp}, \tag{68}$$

where

$$\Lambda_{\mathbf{m}}(x^1, x^2, \lambda) = \frac{(1-\lambda^2)^2}{\lambda^2} \int_0^{\tau_{b\mathbf{m}}} \frac{d\hat{\tau} \lambda'^2}{1 - \lambda'^2} \tag{69}$$

does not depend on p. Here λ and λ' denote the starting value on the cut and the value on the trajectory, respectively. Since D_C^{pp} and $D_C^{\lambda\lambda}$ do not depend on λ and their dependence on x^1 and x^2 originates from dependencies on the background particle density n and on the temperature T, the necessary storage is three-dimensional. (The explicit form of these coefficients can be found, e.g., in Ref. 16.) This is true also for the components of the deviation (24). Thus, the storage requirement for the ''stochastic'' parameters of the map is also reduced to 3D, because complex dependencies of deviation and variance on the momentum modulus can be factorized.

In the following, for the computation of the monoenergetic transport coefficients, the collision operator is further simplified by putting $D_C^{pp} = 0$ and $D_C^{\chi\chi} = \nu_\perp / 2$ with $\nu_\perp$ directly prescribed.

IV. APPLICATIONS AND BENCHMARKING

A. Collisionless orbits

In Fig. 11 the footprints of a trapped particle orbit on minimum-B cuts together with Poincaré plots of the magnetic field are shown. It should be mentioned that a particle orbit in general leaves many footprints on Poincarè cuts during a complete revolution in the trapping region (trapped particle) or over the poloidal angle (passing particle)—bounce period in the usual sense. One can observe this from ''splitting'' of the orbit in Fig. 11. With a radial electric field (see Fig. 12), trapped orbits are closed, as expected. One can also see in both figures that the shapes of orbits obtained from mapping and obtained from direct orbit tracing are practically the same. On the other hand, from the evolution of the pitch angle with time shown in Figs. 13 and 14 it is seen that the orbits are different. They coincide with each other for a limited time only. The reason for this is that the given orbit belongs to a particle going through a few transitions between different trapping states. First it starts with a

FIG. 10. Variance of λ, $\langle \delta \lambda^2 \rangle$, versus λ after one ''bounce'' time. The ratio between connection length and mean-free-path is 10^{-4}.
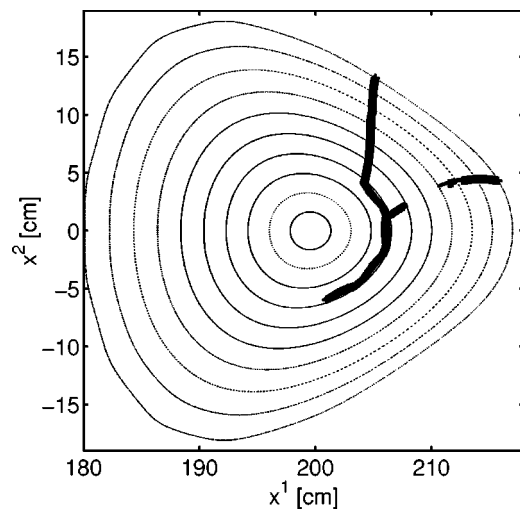
FIG. 11. Footprints of a trapped particle orbit on minimum-B cuts together with Poincaré plots of the magnetic field. The starting values are $\lambda = 0.2$ and $w_k = 8$ keV at the position $x^1 = 206$ cm, $x^2 = 0.01$ cm without a radial electric field. Comparison between direct computation (dots) and mapping procedure (+).

FIG. 13. Time evolution of particle pitch λ for a trapped particle with starting values as given in Fig. 11 without a radial electric field. Comparison between direct computation (dots) and mapping procedure (+).

''toroidal banana orbit'' crossing 7 minima during a complete bounce period, then it becomes blocked within three minima and drifts out of the system. This is better seen from Fig. 15 where the time evolution of the flux label is shown. Such kind of orbits are unstable in the sense that the moment of transition can be strongly influenced even by small errors. On the other hand, these errors are anyway well below the stochastic modifactions of orbits by Coulomb collisions.

Some orbits of trapped particles in QHS are shown in Fig. 16. Due to quasi-helical symmetry, the poloidal drift velocity in this device is much higher than the radial drift velocity. Therefore, almost all these orbits are super-bananas which can be very fat and sometimes those orbits are not closed within the confinement region. The thickness of these orbits is shown in Fig. 17 as function of the particle pitch. The two peaks in this plot correspond to particles with maxi-
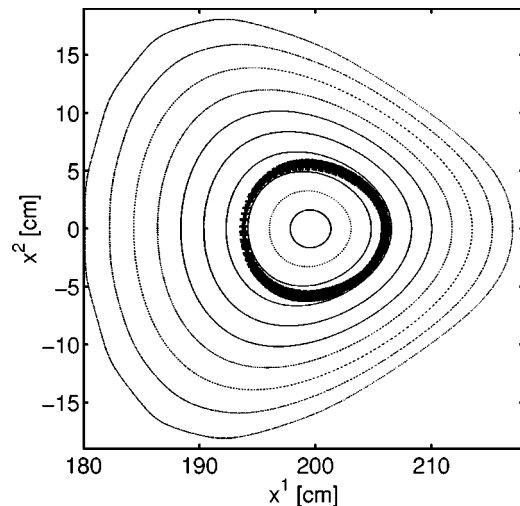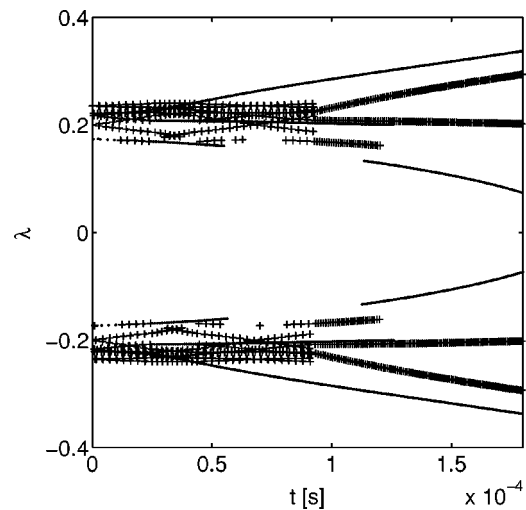
mum deviation towards the center and towards the last closed magnetic surface, respectively. With the help of the mapping technique, the computation of collision less orbits is sufficiently fast to scan the whole phase space volume for the presence of a loss cone. This could be of interest for α-particle confinement studies.

B. Calculation of Green's functions

In various applications of solvers for the DKE, the problem can be reduced to the computation of Green's functions of various types. Such applications are, e.g., the computation of neoclassical transport coefficients,[1] the computation of quasi-stationary nonlocal (convective) fluxes and of power re-deposition profiles of supra-thermal particles generated by radiofrequency heating.[7–9] This results in two types of problems, initial value problems and stationary problems. By definition, these Green's functions $G(\mathbf{z}_0, \mathbf{z})$ satisfy the drift-kinetic equation (1) with δ-function source terms specified as
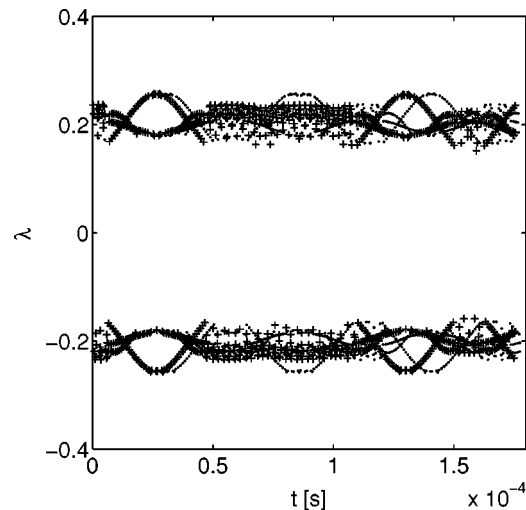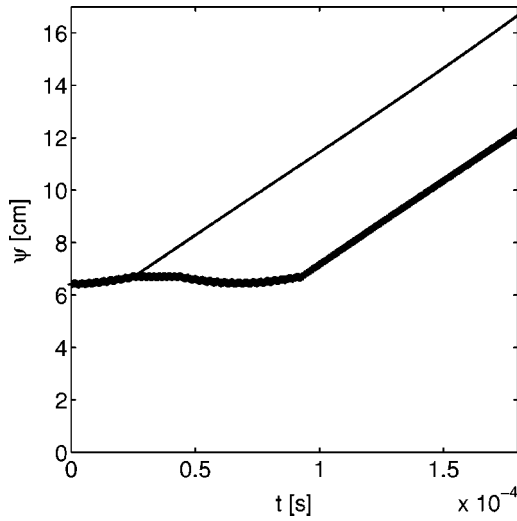

FIG. 12. Same as Fig. 11 with the presence of a radial electric field $E_r = 393$ V/cm.

FIG. 14. Same as Fig. 13 with the presence of a radial electric field $E_r = 393$ V/cm.

Phys. Plasmas, Vol. 9, No. 8, August 2002

Mapping technique for stellarators   3519

FIG. 15. Time evolution of flux label ψ without electric field.

FIG. 17. Maximum particle deviation over the flux label from the starting magnetic surface vs particle pitch for QHS. Same starting values as in Fig. 16.

$$Q_{\text{init}}(\mathbf{z}) = \frac{1}{2\pi J(\mathbf{z})} \delta(\mathbf{z} - \mathbf{z}_0), \tag{70}$$

$$Q_{\text{stat}}(\mathbf{z}) = \frac{\nu_{\text{stat}}}{2\pi J(\mathbf{z})} \delta(z^1 - z_0^1) \cdots \delta(z^5 - z_0^5), \tag{71}$$

for an initial value problem and a stationary problem, respectively, where ν_{stat} is a constant source rate. In addition, homogeneous boundary conditions of various types have to be met.

Assuming that there exists no flux of incoming particles through the outer boundary of the plasma, one boundary condition is

$$V^i(\mathbf{z}) G(\mathbf{z}_0, \mathbf{z}) \frac{\partial \Phi_{\text{bou}}(\mathbf{z})}{\partial z^i} \bigg|_{\Phi_{\text{bou}}(\mathbf{z})=0} = 0$$

$$\text{for} \quad V^i(\mathbf{z}) \frac{\partial \Phi_{\text{bou}}(\mathbf{z})}{\partial z^i} < 0, \tag{72}$$
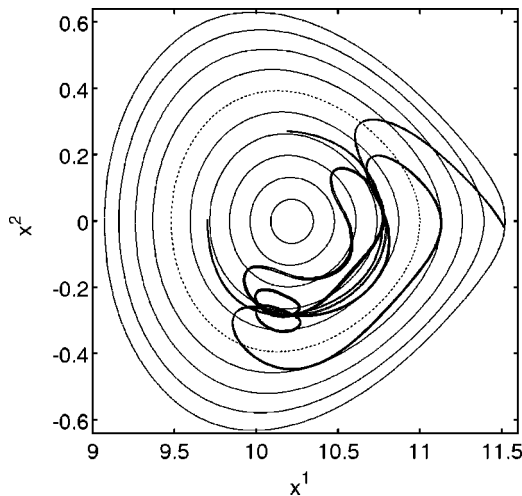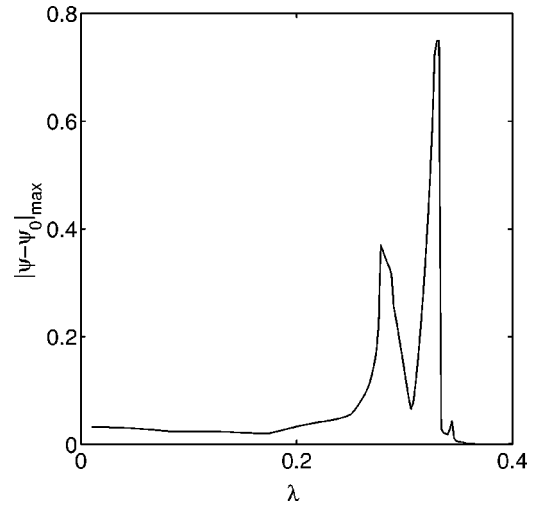

FIG. 16. Footprints of orbits in QHS with starting point position $x^1 = 10.217$ and $x^2 = -0.28$ and Larmor radius $\rho_0 = 0.001$.

where $\Phi_{\text{bou}}(\mathbf{z}) = 0$ is the equation for a boundary surface such that $\nabla \Phi_{\text{bou}}$ is the normal to this surface. In the case of embedded magnetic surfaces, $\Phi_{\text{bou}} = \psi - \psi_b$ where ψ_b is the flux label of the boundary magnetic surface.

In momentum space, boundary conditions follow from the absence of a particle flux through the boundaries $\Phi_{\mathbf{p}}(\mathbf{z}) = 0$. Namely, the physical domain in momentum space is limited by $\Phi_{\mathbf{p}}(\mathbf{z}) = z^4(1 - (z^5)^2)$, and the appropriate boundary condition is given as

$$\left(D^{ij} \frac{\partial G}{\partial z^j} - (V^i + F^i) G \right) \frac{\partial \Phi_{\mathbf{p}}(\mathbf{z})}{\partial z^i} \bigg|_{\Phi_{\mathbf{p}}(\mathbf{z})=0} = 0. \tag{73}$$

In addition, G is limited at infinity, $\lim_{z^4 \to \infty} G = 0$. For the computation of convective losses, additional boundary condition may be required in the thermal region

$$G(\mathbf{z}_0, \mathbf{z})|_{\Phi_{\text{T}}(\mathbf{z})=0} = 0, \tag{74}$$

where $\Phi_{\text{T}}(\mathbf{z}) = z^4 - p_T$, and $p_T = (2m_0 T)^{1/2}$.

All boundary conditions formally result in a specific modification of the kernel in the integral equation (17). Conditions (72) and (74) provide the additional factors $\Theta(\Phi_{\text{bou}}(\mathbf{z}_{\mathbf{m}'}(\mathbf{u}')))$ and $\Theta(\Phi_{\mathbf{p}}(\mathbf{z}_{\mathbf{m}'}(\mathbf{u}')))$, respectively, where $\Theta(x)$ is a Heaviside step function.

The consequence for Monte Carlo operators is that test particles which cross the respective boundary are deleted and that the Markov chain is terminated. In addition, for time depending problems, the termination of Markov chains with time [additional factor $\Theta(t_e - z^5 + z_0^5)$ in the kernel] is introduced where t_e is the the evolution time. Boundary conditions in momentum space (73) can be realized in Monte Carlo operators, e.g., by reflecting test particles from the corresponding boundary.

Integration of δ-functions along unperturbed orbits using (A3) gives

$$J_{\mathbf{m}}(\mathbf{u}) \int_0^{\tau_{b\mathbf{m}}} d\tau \frac{1}{J(\mathbf{Z}(\mathbf{z_m}(\mathbf{u}), \tau))}$$

$$\times \delta(Z^1(\mathbf{z_m}(\mathbf{u}), \tau) - z_0^1) \cdots \delta(Z^5(\mathbf{z_m}(\mathbf{u}), \tau) - z_0^5)$$

$$= J_{\mathbf{m}}(\mathbf{u}) \int_0^{\tau_{b\mathbf{m}}} d\tau \frac{1}{J(\mathbf{Z})} \frac{\partial(\mathbf{z}_L)}{\partial(\mathbf{Z})}$$

$$\times \delta(u^1 - u_0^1(\mathbf{z}_0)) \cdots \delta(u^4 - u_0^4(\mathbf{z}_0)) \delta(\tau - \tau_0(\mathbf{z}_0))$$

$$= \delta(u^1 - u_0^1(\mathbf{z}_0)) \cdots \delta(u^4 - u_0^4(\mathbf{z}_0)). \tag{75}$$

The Lagrangian variables $\mathbf{z}_L$ are defined in Appendix A, and u_0^i and τ_0 are the solutions of the equation set $Z^i(\mathbf{z_m}(\mathbf{u}), \tau) = z_0^i$, $i = 1, \ldots, 5$, which gives the projection of the source point $\mathbf{z}_0$ onto the Poincaré cut along the orbit. Thus, the orbit integrated sources (19), $\mathcal{Q}_{\mathbf{m}}$, are obtained from (70) and (71) as

$$\mathcal{Q}_{\mathbf{m}}^{init}(\mathbf{u}) = \frac{1}{2\pi} \delta(\mathbf{u} - \mathbf{u}_0),$$

$$\mathcal{Q}_{\mathbf{m}}^{stat}(\mathbf{u}) = \frac{\nu_{stat}}{2\pi} \delta(u^1 - u_0^1) \cdots \delta(u^4 - u_0^4), \tag{76}$$

respectively. This kind of source have an intuitively obvious realization in the Monte Carlo algorithm, resulting in the fact that Markov chains are started in the projection point on Poincaré cuts. For an initial value problem, the starting time of evolution, u^5, is τ_0 and the test particle weight is $(2\pi)^{-1}$. For a stationary problem, the starting weight is $(2\pi)^{-1} \nu_{stat}$ and the time variable u^5 is ignored.

C. Transport coefficients

For computation of transport coefficients, an initial value problem corresponding to the source (70) at the initial time moment $z_0^6 = 0$ is considered. Here, the Green's function G itself is not of interest, but a moment of this function, namely the variance of the flux label, $\langle (\psi - \psi_0)^2 \rangle_{\mathbf{rp}} \equiv 2\pi \int d^5 z (\psi(\mathbf{z}) - \psi_0)^2 G(\mathbf{z}_0, \mathbf{z})$, where $\psi_0 = \psi(\mathbf{z}_0)$, is calculated as function of the evolution time $t_e = z^6$. The perpendicular diffusion coefficient is estimated as[1] $D_\perp = \langle (\psi - \psi_0)^2 \rangle_{\mathbf{rp}}/(2t_e)$. Substituting $A(\mathbf{z}) = (\psi(\mathbf{z}) - \psi_0)^2 \delta(z^6 - t_e)$ in (28) and ignoring the change in $\psi(\mathbf{z})$ during a single bounce time, one obtains

$$\langle (\psi - \psi_0)^2 \rangle_{\mathbf{rp}} = 2\pi \sum_{\mathbf{m}} \int d^5 u \, \Gamma_{\mathbf{m}}(\mathbf{u})(\psi(\mathbf{z_m}(\mathbf{u})) - \psi_0)^2$$

$$\times \int_0^{\tau_{\mathbf{m}}(\mathbf{u})} d\tau \delta(\tau + u^5 - t_e)$$

$$= \sum_{k=1}^{\infty} \langle (\psi(\mathbf{z}_{\mathbf{m}_k}(\mathbf{u}_k)) - \psi_0)^2 \Theta(u^5 - t_e)$$

$$\times \Theta(t_e + \tau_{b\mathbf{m}_k}(\mathbf{u}_k) - u^5) \rangle. \tag{77}$$

Here, Eq. (39) has been used to present the variance of the flux label in the form of a statistical average over Markov chains, $(\mathbf{m}_k, \mathbf{u}_k, w_k)$, where test particle weights, $w_k = (2\pi)^{-1}$, stay constant in absence of sinks in phase space, $\nu_0 = 0$. Thus, within the Monte Carlo algorithm, the contri-
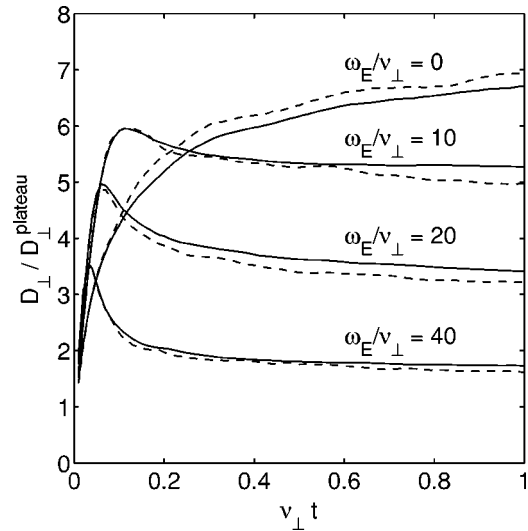

FIG. 18. Normalized diffusion coefficient $D_\perp / D_\perp^{plateau}$ vs time in units of τ_C for different values of normalized rotation frequency (W7-AS). Results from mapping (solid) and direct MC (dashed).

bution of a given test particle to the value of $(\psi - \psi_0)^2$ is computed when the time variable u^5 exceeds t_e.

In the following, the flux label ψ is defined as the value of the big radius R of the flux surface point on the outer side of torus with $Z = 0$ in the symmetric cross-section $\varphi = 0$. The magnetic axis position is given by $\psi = R_0$.

The stochastic mapping technique has been benchmarked against the conventional MC method in regimes with and without radial electric field and against the field-line integration method[17] for evaluating transport coefficients in the $1/\nu$ regime. For both MC procedures, a simplified Lorentz collision operator describing only pitch-angle scattering has been used. The long-mean-free-path regime has been considered with $L_c/l = 0.003$ where $L_c = 2\pi R_0/\iota$ and $l = v/\nu_\perp$ are the connection length and the mean-free path, respectively. Here $\nu_\perp$ is the perpendicular scattering frequency. The computed diffusion coefficient has been normalized to the mono-energetic plateau diffusion coefficient, $D_\perp^{plateau} = \pi \rho_L^2 v/(16\iota R_0)$, where $\rho_L = v/\omega_c$ is the gyro-radius. The radial electric field profile was chosen to keep the electric rotation frequency $\omega_E = c(d\Phi/dr)/(rB)$ close to a constant along the small radius $r \equiv \psi - R_0$. Results for the normalized diffusion coefficient as function of a normalized evolution time t_e/τ_C are shown in Fig. 18 for the W7-AS case. The difference between the results of direct MC and stochastic mapping is mainly due to the statistical error in direct MC. The number of test particles was 10^4 and 10^5, respectively.

For benchmarking with the field line integration technique the "effective ripple amplitude" $\epsilon_{eff}^{3/2}$ has been calculated as

$$\epsilon_{eff}^{3/2} = \frac{9\pi \nu_\perp D_\perp R_0^2}{\sqrt{8} v^2 \rho_L^2} \langle |\nabla \psi| \rangle_{M.S.}^{-2}, \tag{78}$$

where $D_\perp$ was evaluated for the $1/\nu$-regime (zero radial electric field). Here $\langle \cdots \rangle_{M.S.}$ is an average over the volume between two close magnetic surfaces. For an arbitrary stellar-
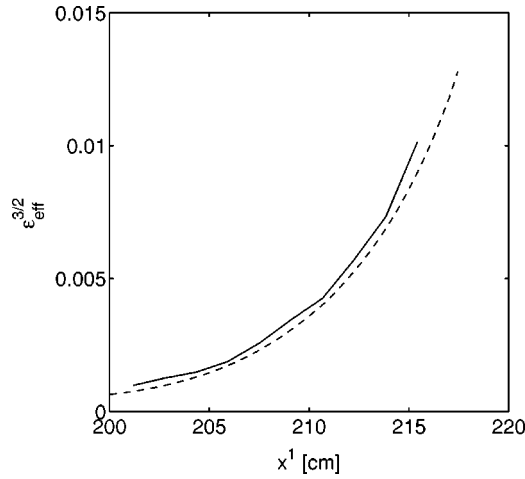
FIG. 19. Effective ripple amplitude $\epsilon_{\mathrm{eff}}^{3/2}$ vs major radius x^1 (W7-AS). Results from mapping (solid) and from field line integration (dashed) are given.

ator, ϵ_{eff} is substituted for the helical ripple amplitude ϵ_h in formulas for $1/\nu$ transport coefficients for the standard stellarator. In Fig. 19 the effective ripple amplitude $\epsilon_{\mathrm{eff}}^{3/2}$ is plotted versus the major radius for W7-AS whereas the result for QHS is given in Fig. 20. The results from the mapping approach and from the field line integration stay in good agreement. It should be mentioned here that for QHS the computation of $1/\nu$ losses with MC procedures is rather delicate since, on one hand, very low-collision frequencies have to be chosen in order to avoid symmetric losses and, on the other hand, it has to be ensured that the interpolation procedures in the SMT code do not destroy the quasi-helical symmetry.

D. Stationary Green's functions

In order to separate the problem of finding the distribution function of supra-thermal electrons generated by localized electron cyclotron resonance heating (ECRH) from the problem of computing the particle and energy balance,
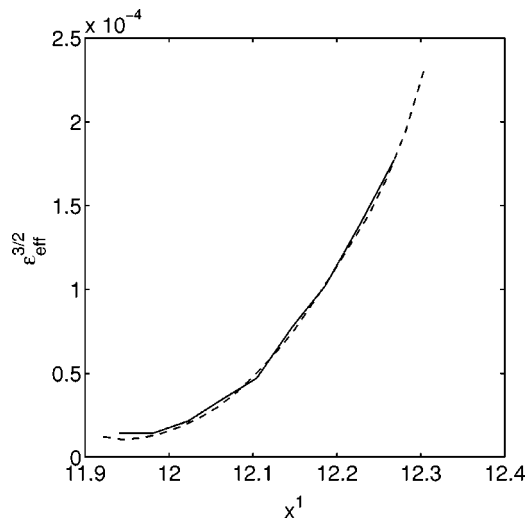

FIG. 20. Effective ripple amplitude $\epsilon_{\mathrm{eff}}^{3/2}$ vs major radius x^1 (QHS). Results from mapping (solid) and from field line integration (dashed) are given.

linear[8] or nonlinear[18] δf methods are used in the kinetic modeling. Within these methods, the electron distribution function f is formally split into two parts, $f = f_0 + \delta f$, where f_0 is the unperturbed distribution function of bulk electrons and δf is the non-Maxwellian part of special interest. The kinetic equation is presented in a symbolic form

$$V^i \frac{\partial f}{\partial z^i} = \hat{L}_C f + \hat{L}_{RF} f, \tag{79}$$

where $\hat{L}_C$ is the Coulomb collision operator describing collisions with background ions and with electrons, and $\hat{L}_{RF}$ is an operator describing the wave–particle interaction. In case of small enough wave amplitudes, this operator is given by quasi-linear theory.[19] Using the separation of f into f_0 and δf in (79), the equation for δf is given as

$$V^i \frac{\partial \delta f}{\partial z^i} - \hat{L}_C \delta f - \hat{L}_{RF} \delta f + \nu_{\mathrm{eff}} \delta f = \hat{L}_{RF} f_0, \tag{80}$$

where ν_{eff} is some effective exchange frequency which is taken to be small in the supra-thermal range of energies.

If the total amount of supra-thermal electrons is small, the kinetic equation for f_0 together with the assumption of a local Maxwellian distribution function leads to a set of one-dimensional neoclassical transport equations, which contain additional magnetic surface averaged source terms of particles Q_n and energy Q_w

$$Q_n = \left\langle \int d^3 p\, \nu_{\mathrm{eff}} \delta f \right\rangle_{M.S.} = -\frac{1}{S} \frac{\partial \Gamma_{n\perp}}{\partial \psi},$$

$$Q_w = \left\langle \int d^3 p\, w_k (\hat{L}_C \delta f + \nu_{\mathrm{eff}} \delta f) \right\rangle_{M.S.}$$

$$= \left\langle \int d^3 p\, w_k \hat{L}_C \delta f \right\rangle_{M.S.} - \frac{1}{S} \frac{\partial \Gamma_{w\perp}}{\partial \psi}. \tag{81}$$

Here $w_k = m_0 c^2 (\gamma - 1)$, S, $\Gamma_{n\perp}$ and $\Gamma_{w\perp}$ are the kinetic energy, magnetic surface area, total fluxes of supra-thermal particles and energy, respectively. Without the quasi-linear operator on the left-hand side of (80), this procedure reduces to the linear Green's function approach given in Refs. 9 and 8. This approach is valid if $\delta f \ll f_0$ in the whole phase space and leads to a linear scaling of δf with ECRH input power. Within this approach, δf is expressed through a Green's function corresponding to (71) as

$$\delta f(\mathbf{z}) = 2\pi \int d_0^5 J(\mathbf{z}_0) G(\mathbf{z}_0, \mathbf{z}) \hat{L}_{RF} f_0(\mathbf{z}_0), \tag{82}$$

with $\nu_{\mathrm{stat}} = 1$.

The supra-thermal particle flux, $\Gamma_{n\perp}$, is of particular importance for the confinement since it can strongly influence the radial electric field through the ambipolarity condition.[7] Note that the procedure for finding the self-consistent radial electric field requires the iterations of this field and, therefore, a relatively fast evaluation of the supra-thermal particle flux $\Gamma_{n\perp}$ is necessary. The usual expression for particle flux defined in guiding center variables and flux coordinates (ψ, θ, φ) can be transformed to the average over the Poincaré cuts as follows:

$$\Gamma_{n\perp}(\psi_0) = \int d^3p \int_{-\pi}^{\pi} d\theta \int_{-\pi}^{\pi} d\varphi \, \frac{\mathbf{v}_g \cdot \nabla \psi}{|\nabla \psi|} \left| \frac{\partial \mathbf{r}}{\partial \theta} \times \frac{\partial \mathbf{r}}{\partial \varphi} \right| f$$

$$= \int d^3p \int_{-\pi}^{\pi} d\theta \int_{-\pi}^{\pi} d\varphi \int d\psi' \, \delta(\psi' - \psi_0) \sqrt{g} f \mathbf{v}_g$$

$$\cdot \nabla \psi$$

$$= \int d^3p \int d^3r \, \delta(\psi' - \psi_0) f \mathbf{v}_g \cdot \nabla \psi$$

$$= 2\pi \sum_{\mathbf{m}} \int d^5u \, \Gamma_{\mathbf{m}}(\mathbf{u}) \, \delta(t - u^5) \int_0^{\tau_{b\mathbf{m}}} d\tau$$

$$\times \delta(\psi(\mathbf{Z}(\mathbf{z_m}, \tau)) - \psi_0) \mathbf{v}_g \cdot \nabla \psi|_{\mathbf{z} = \mathbf{Z}(\mathbf{z_m}, \tau)}$$

$$= 2\pi \sum_{\mathbf{m}} \int d^5u \, \Gamma_{\mathbf{m}}(\mathbf{u}) \, \delta(t - u^5)$$

$$\times [\Theta(\psi(\mathbf{Z}(\mathbf{z_m}, \tau_{b\mathbf{m}})) - \psi_0) - \Theta(\psi(\mathbf{Z}(\mathbf{z_m}, 0)))$$

$$- \psi_0)]. \tag{83}$$

Here, when integrating over τ, Eqs. (14) for the particle orbits have been used. The energy flux is obtained in the same way and it differs form $\Gamma_{n\perp}$ by the factor $w_k(\mathbf{u})$ in the subintegrand.

Expression (83) does again mean an intuitively obvious procedure for the evaluation of total fluxes (see also Ref. 6). When the particle crosses a surface labeled with ψ, its weight is either added to or subtracted from the value of the flux on a given surface depending on the direction of the crossing.

The particular form of the exchange frequency ν_{eff} in the thermal range of energies has little consequences for the result. In the present modeling, it is assumed to be infinite for energies $w_k < T$ and equal to zero for $w_k > T$. This particular case of ν_{eff} is realized with an additional boundary condition for the Green's function, Eq. (74), and the second expressions in (81) have to be used.

In Figs. 21 and 22, particle and energy fluxes of supra-thermal particles are shown, respectively. The particle source is on the magnetic axis in the magnetic field minimum located at the elliptic cross section of W7-AS. Trapped particles with a pitch value $\lambda = 0.1$ and fixed energies w_0 ranging from $w_0 = 2T_{e0}$ to $w_0 = 9T_{e0}$ are generated there. Thus, the supra-thermal particle distribution function is a stationary Green's function corresponding to (71). The source rate in these computations was $\nu_{\text{stat}} = P_{\text{source}}/w_0$ where $P_{\text{source}} = 400$ kW is the source power. The profiles of the equilibrium parameters were the following, $T_e(r) = T_{e0}(1.2 - (r/a)^2)$, $n_e(r) = n_{e0}(1.2 - (r/a)^2)^2$, $\Phi(r) = T_{e0}r^2/(ea^2)$, where $T_{e0} = 3$ keV, $n_{e0} = 3 \cdot 10^{13}$ cm^{-3}, and $a = 17.4$ cm, respectively. The computation of one such profile requires from minutes to tens of minutes on a DEC Alphastation 500 depending on accuracy. Therefore, iterations of the radial electric field in presence of a supra-thermal particle flux are possible. From those figures one can also see, that rescaling of the Larmor radius and of the collision operator has practically no effect on the results.
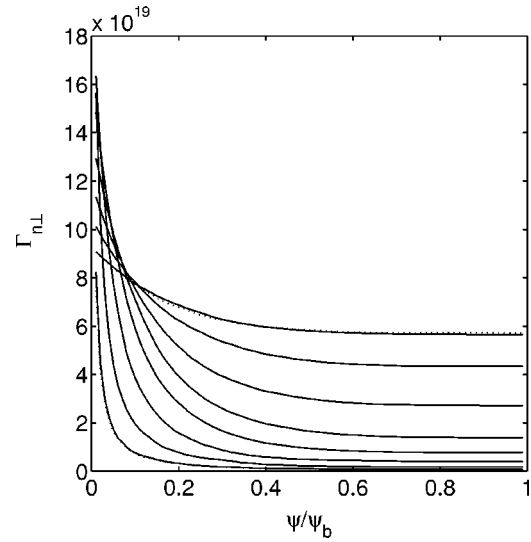

FIG. 21. Particle flux $\Gamma_{n\perp}$ vs normalized flux label ψ/ψ_b. The particle energy ranges from $w_0 = 2T_{e0}$ to $w_0 = 9T_{e0}$ from bottom to top. The dotted lines are computed with Larmor radius and collision operator reduced by a factor of 2.

V. SUMMARY

In the present paper, the stochastic mapping technique has been developed and realized in a numerical code. With the help of this technique, the drift kinetic equation is solved in the long-mean-free-path regime for a stellarator with arbitrary geometry and topology of the magnetic field, allowing also for islands and ergodic magnetic-field layers. The technique has been benchmarked against conventional Monte Carlo methods. The regimes with and without a radial electric field are well reproduced. On the other hand, the mapping procedure is significantly faster (2 and more orders of magnitude depending on the complexity of the magnetic field). Note that the speed of the mapping solver is practically independent of the complexity and computational cost of the magnetic field, therefore, the gain will be even more significant for configurations with a broad magnetic-field
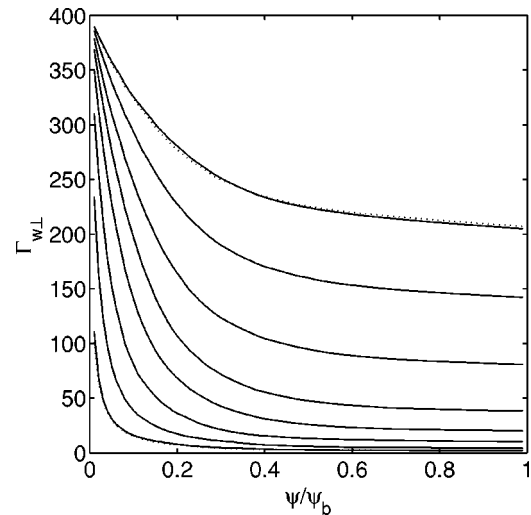

FIG. 22. Energy flux $\Gamma_{w\perp}$ vs normalized flux label ψ/ψ_b (same values of energy as in Fig. 21).

spectrum. Since the preloading procedure is relatively time consuming, the method is most effective in a case when "global" computations of the particle distribution function are needed, e.g., for the studies of kinetic effects of rf-heating, or for the computation of profiles of transport coefficients for fixed magnetic configurations. The comparison with effective ripple computations using the field line integration technique shows that even for the very sensitive quasi-helically symmetric configuration, the errors of drift orbits in SMT are very small.

The application of SMT to a global computation of supra-thermal particle fluxes in a stellarator shows that this method is fast enough to allow for iterations of the radial electric field using the ambipolarity condition taking into account fluxes from supra-thermal particles. Therefore, the SMT combined with a neoclassical balance code will permit the self-consistent modeling of particle and energy balance in a stellarator with strong electron or ion cyclotron heating where the convective transport of supra-thermal particles plays a significant role. At the same time, it is shown that convective fluxes are very sensitive to the detailed structure of the supra-thermal particle source. In the case of ECRH, nonlinear effects of wave–particle interaction are dominant in the formation of such a source.[20] The method for modeling this effects has been recently developed and will be included in future models based on SMT.

ACKNOWLEDGMENTS

APPENDIX A: STOCHASTIC MAPPING EQUATION

Using the fact that trajectories, $\mathbf{Z}(\mathbf{z}, \tau)$, are solutions to (14), one can transform the DKE (1) to a set of Lagrangian variables $\mathbf{z}_L \equiv (\mathbf{u}, \tau)$, introduced as follows:

$$z^i = Z^i(\mathbf{z_m}, \tau), \tag{A1}$$

where the set $\mathbf{z_m} = \mathbf{z_m}(\mathbf{u})$ is defined in the text after (14). Equation (1) takes the form

$$\frac{\partial f}{\partial \tau} = \frac{1}{J_\mathbf{m}} \frac{\partial}{\partial z_L^i} J_\mathbf{m} \left(D_\mathbf{m}^{ij} \frac{\partial f}{\partial z_L^j} - F_\mathbf{m}^i f \right) - \nu f + Q, \tag{A2}$$

where

$$J_\mathbf{m} = J(\mathbf{z}) \frac{\partial(\mathbf{z})}{\partial(\mathbf{z}_L)} = J_\mathbf{m}(\mathbf{u}) \tag{A3}$$

is the Jacobian of coordinate set $\mathbf{z}_L$ given by (18). The Jacobian (A3) is independent of τ. The components of the diffusion tensor and the drag force are transformed according to the rules of tensor algebra,

$$D_\mathbf{m}^{ij} = \bar{c}_k^i \bar{c}_l^j D^{kl}, \quad F_\mathbf{m}^i = \bar{c}_k^i F^k, \tag{A4}$$

where the transformation coefficients $c_k^i \equiv \partial z_L^i / \partial z^k$ satisfy (26) and (27). The bounce time, $\tau_{b\mathbf{m}}(\mathbf{u})$, can be introduced as the smallest nontrivial solution of the equation

$$\Phi_{\mathbf{m}'}(\mathbf{Z}(\mathbf{z}_m, \tau_{b\mathbf{m}})) = 0, \tag{A5}$$

with respect to τ. Here, $\mathbf{m}'$ labels all possible cuts. It corresponds to the change in the trajectory parameter τ needed to reach the nearest cut along the orbit. This can be the same cut as the initial one if the orbit belongs to a "trapped" particle. The particular value of the index $\mathbf{m}'$ corresponding to this solution defines a discrete mapping $\mathbf{m}' = \mathbf{M_m}(\mathbf{u})$ in Eq. (13). In the long-mean-free-path regime, the distribution function changes only weakly during the bounce time, i.e., within the interval $0 < \tau < \tau_{b\mathbf{m}}$. Therefore, Eq. (A2) can be integrated over τ from 0 to $\tau_{b\mathbf{m}}$ assuming that the distribution function f on the right-hand side is independent of τ. This results in

$$\Gamma_{\mathbf{m}'}(\mathbf{u}') \frac{\partial(\mathbf{u}')}{\partial(\mathbf{u})} = \Gamma_\mathbf{m}(\mathbf{u}) + \frac{\partial}{\partial u^i \partial u^j} \bar{D}_\mathbf{m}^{ij}(\mathbf{u}) \Gamma_\mathbf{m}(\mathbf{u})$$

$$- \frac{\partial}{\partial u^i} \mathcal{F}_\mathbf{m}^i(\mathbf{u}) \Gamma_\mathbf{m}(\mathbf{u}) - \bar{\nu}_\mathbf{m}(\mathbf{u})$$

$$+ \mathcal{Q}_\mathbf{m}(\mathbf{u}), \tag{A6}$$

where $\mathbf{m}'$ and $\mathbf{u}'$ are given by (13), and the rest of the notation is given by (17)–(25). Since the terms neglected on the right-hand side of (A6) are quadratic with respect to the small parameter $\tau_{b\mathbf{m}}/\tau_c$ where τ_c is the collision time, with the same accuracy one can replace the right-hand side with the integral

$$\Gamma_{\mathbf{m}'}(\mathbf{u}') \frac{\partial(\mathbf{u}')}{\partial(\mathbf{u})} = \int d^5 u'' \langle \delta(\mathbf{u}'' - \mathbf{u} + \delta\mathbf{u}(\mathbf{u}'')) \rangle$$

$$\times (1 - \bar{\nu}_\mathbf{m}(\mathbf{u}''))(\Gamma_\mathbf{m}(\mathbf{u}'') - \mathcal{Q}_\mathbf{m}(\mathbf{u}'')), \tag{A7}$$

where $\delta\mathbf{u}(\mathbf{u}'')$ are small random numbers satisfying (20). It should be mentioned that the quantities $\bar{\nu}_\mathbf{m}$ and $\mathcal{Q}_\mathbf{m}$ are small in the first order over $\tau_{b\mathbf{m}}/\tau_c$. Transforming the δ-function with the help of

$$\delta(\mathbf{u}'' - \mathbf{u} + \delta\mathbf{u}(\mathbf{u}'')) = \frac{\partial(\mathbf{U_m}(\mathbf{u}))}{\partial(\mathbf{u})}$$

$$\times \delta(\mathbf{U_m}(\mathbf{u}) - \mathbf{U_m}(\mathbf{u}'' + \delta\mathbf{u}(\mathbf{u}''))), \tag{A8}$$

and using (13), which implicitly define $\mathbf{m}$ and $\mathbf{u}$ through $\mathbf{m}'$ and $\mathbf{u}'$, one obtains Eq. (17). Note that in order to simplify the notation in (17), the dummy integration variable $\mathbf{u}''$ was replaced with $\mathbf{u}$.

APPENDIX B: METRIC DETERMINANT OF THE LMCS

In order to obtain the metric determinant $\sqrt{g}$ entering (3), one notices that the only nonzero contravariant component of the magnetic field is $B^3 \equiv \mathbf{B} \cdot \nabla x^3 = B^\varphi$. Using

$$\nabla \cdot \mathbf{B} \equiv \frac{1}{\sqrt{g}} \frac{\partial}{\partial x^i} \sqrt{g} B^i = \frac{1}{\sqrt{g}} \frac{\partial}{\partial x^3} \sqrt{g} B^\varphi = 0, \tag{B1}$$

one obtains that the product $\sqrt{g}B^\varphi$ is constant along a magnetic-field line defined by $(x^1,x^2)=$ const. Since due to (45) and (43) the coordinates x^1 and x^2 coincide with R and Z on the reference cut, $\sqrt{g}=R$ there. Therefore, one obtains

$$\sqrt{g}=\frac{x^1 B^\varphi(x^1,x^2,\varphi_n)}{B^\varphi(R(\mathbf{x}),Z(\mathbf{x}),\varphi(\mathbf{x}))},\tag{B2}$$

where the azimuthal component B^φ is considered in (B2) as a function of cylindrical coordinates and $R(\mathbf{x})$, $Z(\mathbf{x})$, $\varphi(\mathbf{x})$ are cylindrical coordinates of the point on the minimum-B cut, $\varphi=x^3=\vartheta_{\mathbf{m}}(\mathbf{u})$ ($\mathbf{x}$ are magnetic coordinates of this point). In the case of stellarator symmetry $\varphi_n=0$ in (B2). In zero order with respect to the Larmor radius, the particle velocity is along the magnetic field, $\mathbf{v}_g=v_\parallel\mathbf{h}$. Using the definitions of the Jacobian $J_{\mathbf{m}}$ and the hyper-surface $\Phi_{\mathbf{m}}$, Eqs. (18) and (15), respectively, and taking into account that $\mathbf{v}_g\cdot\nabla\vartheta_{\mathbf{m}}=0$, one obtains

$$J_m=\frac{x^1 p^2 v_\parallel B^\varphi(x^1,x^2,\varphi_n)}{B(R(\mathbf{x}),Z(\mathbf{x}),\varphi(\mathbf{x}))}$$

$$=\frac{p^3\lambda\hat{B}_\varphi(x^1,x^2,\varphi_n)}{m_0\gamma B(R(\mathbf{x}),Z(\mathbf{x}),\varphi(\mathbf{x}))}.\tag{B3}$$

Here p and λ are momentum modulus and pitch on the minimum-B cut, respectively, and $\hat{B}_\varphi(R,Z,\varphi)=RB^\varphi(R,Z,\varphi)$ is the physical toroidal component of the magnetic field.

APPENDIX C: MOMENTS AND FLUXES

It is of interest to derive expressions for certain local moments of the distribution function,

$$\langle A\rangle_{\mathbf{p}}\equiv\int d^3 p A f.\tag{C1}$$

These moments of interest are the particle density, the parallel current density and the kinetic-energy density where A is introduced as $A=1$, $A=ev_\parallel$ and $A=m_e c^2(\gamma-1)$, respectively. In order to reconstruct the distribution function and its moments away from a minimum-B cut, one uses the following assumptions. The particle cross-field displacement due to the drift and due to effects of collisions is neglected for the computation of particle orbits during one bounce time. This means that on distances of the order of one magnetic-field period, the distribution function expressed in terms of invariants of motion in the momentum space can be considered constant along the magnetic-field line, i.e., the distribution function in any spatial point is taken to be the same as in the point on the minimum-B cut which has the same values of the magnetic coordinates x^1 and x^2. For the reconstruction at a given point, one has to use this minimum-B cut where there exists no local maximum of B along the magnetic field line between the cut and the given point.

To simplify the notation, one can use $\hat{B}_\varphi=\hat{B}_\varphi(x^1,x^2,\varphi_n)$ for the toroidal physical component of the magnetic field on the reference cut, $B_m=B(\mathbf{x}_m)$ for the magnetic-field modulus on the minimum-B cut, and $B=B(\mathbf{x})$ for the magnetic-field modulus in the considered point. All three quantities belong to the same magnetic-field

line. Furthermore, one can neglect the variation of the electrostatic potential along the field line. This means that the kinetic energy and, as a consequence, p are the approximate constants of motion. Thus one gets

$$f(x^1,x^2,x^3,p,\lambda)=f(x^1,x^2,x_m^3,p,\lambda_m),\tag{C2}$$

with

$$\frac{1-\lambda^2}{B}=\frac{1-\lambda_m^2}{B_m}.\tag{C3}$$

The last expression follows from the conservation of the magnetic moment. For the moments one obtains

$$\langle A\rangle_{\mathbf{p}}=2\pi\int_0^\infty dp\int_{-1}^1 d\lambda\, p^2 A f$$

$$=\int_0^\infty dp\int_{-1}^1 d\lambda_m\Theta(|\lambda_m|-\lambda_b)\frac{2\pi m_e\gamma B}{|\lambda|p\hat{B}_\varphi}A|\Gamma_{\mathbf{m}}|,\tag{C4}$$

where

$$|\lambda|=\sqrt{1-\frac{B}{B_m}(1-\lambda_m^2)},\quad\lambda_b=\sqrt{1-\frac{B_m}{B}}.\tag{C5}$$

In particular, for the parallel current density one gets

$$j_\parallel=\frac{2\pi eB}{\hat{B}_\varphi}\int_0^\infty dp\int_{-1}^1 d\lambda_m\Theta(|\lambda_m|-\lambda_b)|\Gamma_{\mathbf{m}}|\text{sign}(\lambda_m).\tag{C6}$$

Note that neglecting the particle displacements from the field line distorts bootstrap effects in the computation of parallel currents. If this effect is of interest, the full orbit should be used with help of (28) substituting there $A(\mathbf{z})=ev_\parallel(\mathbf{z})\delta(z^1-x^1)\cdots\delta(z^3-x^3)\delta(z^6-t)$.

[1] A. H. Boozer and G. Kuo-Petravic, Phys. Fluids **24**, 851 (1981).
[2] H. Wobig and R. H. Fowler, Plasma Phys. Controlled Fusion **30**, 721 (1988).
[3] A. Montvai and D. F. Düchs, in *Physics Computing '92, Prague, 1992* (World Scientific, Singapore, 1993), p. 417.
[4] M. de Rover, N. J. Lopes Cardozo, and A. Montvai, Phys. Plasmas **3**, 4468 (1996).
[5] S. V. Kasilov, V. E. Moiseenko, and M. F. Heyn, Phys. Plasmas **4**, 2422 (1997).
[6] A. M. Runov, D. Reiter, S. V. Kasilov, W. Kernbichler, and M. F. Heyn, Phys. Plasmas **8**, 916 (2001).
[7] H. Maassberg, C. D. Beidler, U. Gasparino, M. Rome, W.-A. Team, K. S. Dyabilin, N. B. Marushchenko, and S. Murakami, Phys. Plasmas **7**, 295 (2000).
[8] S. Murakami, U. Gasparino, H. Idei, S. Kubo, H. Maassberg, N. Nakajima, M. Rome, and M. Okamoto, Nucl. Fusion **40**, 693 (2000).
[9] M. Romé, V. Erckmann, U. Gasparino, H. Hartfuss, G. Kühner, H. Maassberg, and N. Marushchenko, Plasma Phys. Controlled Fusion **39**, 117 (1997).
[10] W. Dommaschk, W. Lotz, and J. Nührenberg, Nucl. Fusion **24**, 794 (1984).
[11] J. Nührenberg and R. Zille, Phys. Lett. A **129**, 113 (1988).
[12] V. V. Nemov, Phys. Plasmas **6**, 122 (1999).
[13] C. Grebogi and R. G. Littlejohn, Phys. Fluids **27**, 1996 (1984).
[14] A. I. Morozov and L. S. Solov'ev, *Reviews of Plasma Physics* (Consultants Bureau, New York, 1966), Vol. 2, pp. 201–297.
[15] M. H. Kalos and P. A. Whitlock, *Monte Carlo Methods. Volume I: Basics* (Wiley, New York, 1986).
[16] J. N. Dnestrovskij and D. P. Kostomarov, *Numerical Simulation of Plasmas* (Springer Verlag, Berlin, 1986).

[17] V. V. Nemov, S. V. Kasilov, W. Kernbichler, and M. F. Heyn, Phys. Plasmas **6**, 4622 (1999).

[18] S. V. Kasilov, W. Kernbichler, V. V. Nemov, and M. F. Heyn, in *26th EPS Conference on Controlled Fusion and Plasma Physics, Maastricht, 14–18 June 1999. ECA Vol. 23J*, edited by B. Schweer, G. Van Oast, and E. Vietzke (European Physical Society, Mulhouse, 1999), pp. 1629–1632.

[19] S. Kasilov, in *Proceedings of the Seventh European Fusion Theory Conference, 8–10 October 1997, Jülich, Germany*, edited by A. Rogister (Forshungszentrum Jülich GmbH, Jülich, Germany, 1998), pp. 111–114.

[20] M. F. Heyn, S. V. Kasilov, W. Kernbichler, H. Maassberg, M. Romé, U. Gasparino, and N. B. Marushchenko, in *26th EPS Conference on Controlled Fusion and Plasma Physics, Maastricht, 14–18 June 1999. ECA Vol. 23J*, edited by B. Schweer, G. Van Oost, and E. Vietzke (European Physical Society, Mulhouse, 1999), pp. 1625–1628.